# The conserved AAA-ATPase PCH-2$^{TRIP13}$ regulates spindle checkpoint strength

Lénaïg Défachelles, Anna E. Russo, Christian R. Nelson, and Needhi Bhalla*
Department of Molecular, Cell and Developmental Biology, University of California, Santa Cruz, Santa Cruz, CA 95064

**ABSTRACT** **Spindle checkpoint strength is dictated by the number of unattached kinetochores, cell volume, and cell fate. We show that the conserved AAA-ATPase PCH-2/TRIP13, which remodels the checkpoint effector Mad2 from an active conformation to an inactive one, controls checkpoint strength in *Caenorhabditis elegans*. Having previously established that this function is required for spindle checkpoint activation, we demonstrate that in cells genetically manipulated to decrease in cell volume, PCH-2 is no longer required for the spindle checkpoint or recruitment of Mad2 at unattached kinetochores. This role is not limited to large cells: the stronger checkpoint in germline precursor cells also depends on PCH-2. PCH-2 is enriched in germline precursor cells, and this enrichment relies on conserved factors that induce asymmetry in the early embryo. Finally, the stronger checkpoint in germline precursor cells is regulated by CMT-1, the ortholog of p31$^{comet}$, which is required for both PCH-2's localization to unattached kinetochores and its enrichment in germline precursor cells. Thus, PCH-2, likely by regulating the availability of inactive Mad2 at and near unattached kinetochores, governs checkpoint strength. This requirement may be particularly relevant in oocytes and early embryos enlarged for developmental competence, cells that divide in syncytial tissues, and immortal germline cells.**

**Monitoring Editor**
Ahna Skop
University of Wisconsin, Madison

Received: May 15, 2020
Revised: Jul 10, 2020
Accepted: Jul 17, 2020

## INTRODUCTION

To prevent the missegregation of chromosomes and the production of daughter cells with an incorrect number of chromosomes, the spindle checkpoint (also called the spindle assembly checkpoint or the mitotic checkpoint) monitors whether chromosomes are attached to the spindle via kinetochores. If kinetochores fail to attach properly, this checkpoint delays the cell cycle to promote error correction and prevent aneuploidy. Despite its critical role, the duration of the cell cycle delay, defined as the strength of the spindle checkpoint, can be highly variable. This variability can be controlled by the number of unattached kinetochores (Collin *et al.*, 2013), cell volume (Galli and Morgan, 2016; Kyogoku and Kitajima, 2017), and cell fate (Galli and Morgan, 2016; Gerhold *et al.*, 2018).

The spindle checkpoint response is initiated by the recruitment of Mad1 and Mad2 at unattached kinetochores (Chen *et al.*, 1996, 1998; Li and Benezra, 1996; Sironi *et al.*, 2001), which catalyzes the production of a mitotic checkpoint complex (MCC). The MCC enforces a checkpoint arrest by inhibiting the anaphase-promoting complex/cyclosome (APC/C) and preventing cell cycle progression (Sudakin *et al.*, 2001). Formation of the MCC is driven by conformational changes in Mad2, which can exist in an open conformation (O-Mad2) or a closed conformation (C-Mad2; Luo *et al.*, 2002, 2004; Sironi *et al.*, 2002). Mad2 is in the closed conformation in the Mad1/Mad2 tetramer recruited to unattached kinetochores. C-Mad2 in the tetramer acts as a template to convert additional soluble O-Mad2 to C-Mad2, which can be assembled into the MCC (Sironi *et al.*, 2001; De Antoni *et al.*, 2005; Simonetta *et al.*, 2009; Fava *et al.*, 2011). Thus, unattached kinetochores act as a platform for MCC assembly. This soluble signal generated by unattached kinetochores effectively tunes the spindle checkpoint response: the length of the cell cycle delay imposed by the checkpoint is governed by the ratio of unattached kinetochores producing MCC, and its ability to inhibit the APC, to cytoplasmic volume (Collin *et al.*, 2013; Dick and Gerlich, 2013; Galli and Morgan, 2016; Kyogoku and Kitajima, 2017).

This article was published online ahead of print in MBoC in Press (http://www.molbiolcell.org/cgi/doi/10.1091/mbc.E20-05-0310) on July 22, 2020.

Author contributions: L.D., A.E.R., C.R.N., and N.B. provided conceptualization and methodology; L.D., A.E.R., and C.R.N. carried out the investigation; L.D. and N.B. wrote the original draft; L.D., A.E.R., C.R.N., and N.B. revised and edited it; N.B. supervised and acquired funding.

Competing interests: The authors declare no competing interests.

*Address correspondence to: Needhi Bhalla (nbhalla@ucsc.edu).

Abbreviations used: APC/C, anaphase promoting complex/cyclosome; DECON, decondensation; MCC, mitotic checkpoint complex; NEBD, nuclear envelope breakdown; OCC, onset of cortical contractility; RNAi, RNA interference.

| Protein | Mitotic roles in *C. elegans* | Mitotic roles in human cells |
|---|---|---|
| PCH-2/TRIP13 | • Promotes checkpoint function (Nelson *et al.*, 2015)<br>• Regulates Mad2 at unattached kinetochores (Nelson *et al.*, 2015)<br>• No effect on Mad2 protein levels (Nelson *et al.*, 2015)<br>• No effect on checkpoint silencing (this study)<br>• Controls spindle checkpoint strength (this study) | • Promotes checkpoint function (Ma and Poon, 2016; Marks *et al.*, 2017; Yost *et al.*, 2017; Ma and Poon, 2018)<br>• Regulates Mad2 at unattached kinetochores (Yost *et al.*, 2017)<br>• Stabilizes Mad2 protein levels (Ma and Poon, 2016; Marks *et al.*, 2017; Yost *et al.*, 2017)<br>• Silences checkpoint (Eytan *et al.*, 2014; Wang *et al.*, 2014; Miniowitz-Shemtov *et al.*, 2015; Ma and Poon, 2016) |
| CMT-1/p31$^{comet}$ | • Promotes checkpoint function (Nelson *et al.*, 2015)<br>• Regulates Mad2 at unattached kinetochores (Nelson *et al.*, 2015)<br>• Stabilizes Mad2 protein levels (Nelson *et al.*, 2015)<br>• No effect on checkpoint silencing (this study)<br>• Required for PCH-2 localization to unattached kinetochores (Nelson *et al.*, 2015)<br>• Required for PCH-2 enrichment in germline precursor cells during embryogenesis (this study)<br>• Controls spindle checkpoint strength (this study) | • No effect on checkpoint function (Xia *et al.*, 2004; Ma and Poon, 2016)<br>• No effect on Mad2 at kinetochores (Westhorpe *et al.*, 2011)<br>• No effect on Mad2 protein levels (Ma and Poon, 2016)<br>• Silences checkpoint (Habu *et al.*, 2002; Xia *et al.*, 2004; Teichner *et al.*, 2011; Westhorpe *et al.*, 2011) |

**TABLE 1:** Mitotic roles of PCH-2/TRIP13 and CMT-1/p31$^{comet}$.

PCH-2/TRIP13 is a hexameric AAA+ ATPase that remodels HORMA domain-containing proteins, a group that includes Mad2 (Aravind and Koonin, 1998; Rosenberg and Corbett, 2015; Vader, 2015). Biochemical and structural studies have shown that PCH-2 converts C-Mad2 to O-Mad2 (Ye *et al.*, 2015; Brulotte *et al.*, 2017; Alfieri *et al.*, 2018). TRIP13 works with the adaptor protein p31$^{comet}$ to extract C-Mad2 from the MCC and promote its disassembly, permitting the activation of the APC/C and silencing the checkpoint (Eytan *et al.*, 2014; Wang *et al.*, 2014; Miniowitz-Shemtov *et al.*, 2015; Ye *et al.*, 2015; Brulotte *et al.*, 2017; Alfieri *et al.*, 2018). In addition to this role, we and others have shown that PCH-2/TRIP13 is essential for spindle checkpoint activation in *Caenorhabditis elegans* and human cells (Nelson *et al.*, 2015; Ma and Poon, 2016, 2018; Yost *et al.*, 2017). PCH-2 is present at unattached kinetochores (Tipton *et al.*, 2012; Wang *et al.*, 2014; Nelson *et al.*, 2015) and is needed to robustly localize Mad2, but not Mad1, to unattached kinetochores (Nelson *et al.*, 2015; Yost *et al.*, 2017). A major implication of this work is that O-Mad2 can be limiting during checkpoint activation and PCH-2/TRIP13 plays a central role in ensuring its availability (Ma and Poon, 2018).

Based on genetic interaction between the *C. elegans* ortholog of p31$^{comet}$, CMT-1, and PCH-2, we had previously proposed that PCH-2 disassembles a CMT-1/Mad2 complex to promote checkpoint signaling, similarly to its role in checkpoint silencing (Nelson *et al.*, 2015). However, recent data from mammalian systems, in which loss of p31$^{comet}$ does not suppress the requirement for TRIP13 (Nelson *et al.*, 2015; Ma and Poon, 2016, 2018; Yost *et al.*, 2017), and TRIP13's function becomes essential for checkpoint activity only when O-Mad2 becomes limiting (Ma and Poon, 2018), suggest elaborations to this model in *C. elegans*. Given that p31$^{comet}$ binds Mad2, specifically C-Mad2, throughout the cell cycle (Xia *et al.*, 2004; Date *et al.*, 2014) and that CMT-1 is required to maintain Mad2 protein levels (Nelson *et al.*, 2015), we hypothesize that CMT-1's binding of Mad2 plays two roles in *C. elegans*: to stabilize Mad2 and to sequester it until it is required for checkpoint function. In the absence of CMT-1, more O-Mad2 is available despite the reduction in total protein levels, making PCH-2 partially dispensable and explaining the genetic suppression. This model differs from our understanding of TRIP13 and p31$^{comet}$ in cultured human cells (see Table 1), potentially because of the rapidity of embryonic cell cycles, the fact that relative levels of C and O-Mad2 may vary between systems, and the observation that most Mad2 in cultured human cells is present as O-Mad2 (Luo *et al.*, 2004). Further, it highlights the importance of studying spindle checkpoint function in developmentally relevant model organisms.

This model, however, raises another question: if the primary role of PCH-2/TRIP13 is to guarantee that enough O-Mad2 is available for checkpoint activation and this role can be dispensable when enough O-Mad2 is available, is there a reason for PCH-2/TRIP13 to localize to unattached kinetochores (Tipton *et al.*, 2012; Wang *et al.*, 2014; Nelson *et al.*, 2015)? One possible answer comes from our analysis of *cmt-1* mutant worms. In addition to its role as a PCH-2 adapter (Ye *et al.*, 2015) and in stabilizing Mad2 protein levels (Nelson *et al.*, 2015), CMT-1 is also needed to localize PCH-2 to unattached kinetochores during the spindle checkpoint response and generate a robust spindle checkpoint response in AB cells (Nelson *et al.*, 2015). Overexpressing Mad2 does not suppress the partial defect in spindle checkpoint activation in *cmt-1* mutants (Nelson *et al.*, 2015), suggesting that the defect in spindle checkpoint strength is not because of reduced Mad2 protein levels but because of the inability to localize PCH-2 to unattached kinetochores.

Here, we test this possibility and show that PCH-2 controls spindle checkpoint strength in *C. elegans*. Despite being essential for the spindle checkpoint in the large somatic, or AB, cell of the two-cell embryo (Nelson *et al.*, 2015), PCH-2 becomes dispensable for the spindle checkpoint and partially dispensable for Mad2 recruitment at unattached kinetochores as AB cells are genetically manipulated to become smaller. The requirement for PCH-2 in promoting

spindle checkpoint strength is also observed as cells decrease in size during embryogenesis and in germline precursor, or $P_1$ cells, which have a stronger checkpoint than their similarly sized somatic counterparts. PCH-2 is enriched in $P_1$ cells, and this enrichment depends on conserved regulators of embryonic polarity, PAR-1 and PAR-6. Further, the stronger checkpoint in $P_1$ cells also relies on the *C. elegans* ortholog of p31$^{comet}$, CMT-1, indicating that CMT-1's ability to enrich PCH-2 in $P_1$ cells, in addition to its role in localizing PCH-2 to unattached kinetochores, contributes to a stronger checkpoint. We propose that PCH-2 and its mammalian ortholog TRIP13 ensure a robust spindle checkpoint response and proper chromosome segregation by regulating the availability of O-Mad2 at and near unattached kinetochores. This role may be specifically relevant in scenarios where maintaining genomic stability is particularly challenging, such as in oocytes and early embryos enlarged for developmental competence, cells that divide in a syncytium, and germline cells that maintain immortality.

## RESULTS

### PCH-2 becomes dispensable for the spindle checkpoint response in somatic cells experimentally reduced in size

In the large somatic, or AB, cell of the *C. elegans* two-cell embryo, PCH-2 is essential for spindle checkpoint activation (Nelson *et al.*, 2015). To further assess the requirements for PCH-2 function, we manipulated the cell volume of embryos, and thus AB cells, experimentally by performing RNA interference (RNAi) against *ani-2*. *ani-2* encodes a germline-specific anillin whose depletion generates oocytes and, after fertilization, embryos of varying size (Maddox *et al.*, 2005; Figure 1A). We monitored the length of mitosis in these AB cells, using the times of nuclear envelope breakdown (NEBD) and onset of cortical contractility (OCC) as markers for entry into and exit from mitosis, respectively (Essex *et al.*, 2009). We then correlated the length of mitosis to cytoplasmic volume. RNAi of *ani-2* did not affect normal cell cycle progression in controls and *pch-2* and *mad-1* mutants (Supplemental Figure S1A), indicating that reducing cytoplasmic volume did not affect mitotic timing in AB cells. (In *C. elegans*, the genes that encode Mad1 and Mad2 are *mdf-1* and *mdf-2*, respectively. To avoid confusion, we will use *mad-1* and *mad-2*.)

We performed double depletion of *ani-2* and *zyg-1* to induce the spindle checkpoint response in control embryos and *pch-2* and *mad-1* mutants. ZYG-1 is essential for centrosome duplication, and after the first embryonic division, its depletion generates monopolar spindles (O'Connell *et al.*, 2001) and unattached kinetochores (Essex *et al.*, 2009; Figure 1B). Consistent with previous reports, as AB cells decreased in cell volume, the length of the cell cycle delay, an indicator of spindle checkpoint strength, increased in control embryos (Galli and Morgan, 2016; Gerhold *et al.*, 2018; Figure 1C; Supplemental Videos 1 and 2). Surprisingly, as *pch-2* mutants decreased in size, the spindle checkpoint response resembled that of control AB cells more closely than *mad-1* mutants (Figure 1C; Supplemental Videos 3 and 4). *mad-1* mutant embryos appear more sensitive to *ani-2* RNAi treatment, and we had difficulty recovering any wild type–sized *mad-1* embryos. There was no significant difference between the slopes of the regression analysis of control and *pch-2* mutant data ($p = 0.4664$), while the slopes between the regression analyses of *pch-2* and *mad-1* mutant data were significantly different ($p = 0.0007$).

To make these comparisons more clear, we binned our data. By our measurements, control AB cells ranged from 5 to $6 \times 10^3$ µm$^3$. Therefore, we classified AB cells larger than $5 \times 10^3$ µm$^3$ as wild type–sized. *ani-2$^{RNAi}$;zyg-1$^{RNAi}$* AB cells that were wild type–sized exhibited mitotic delays, while similarly sized *pch-2;ani-2$^{RNAi}$;zyg-1$^{RNAi}$* mutants produced no checkpoint response (Figure 1D). These data

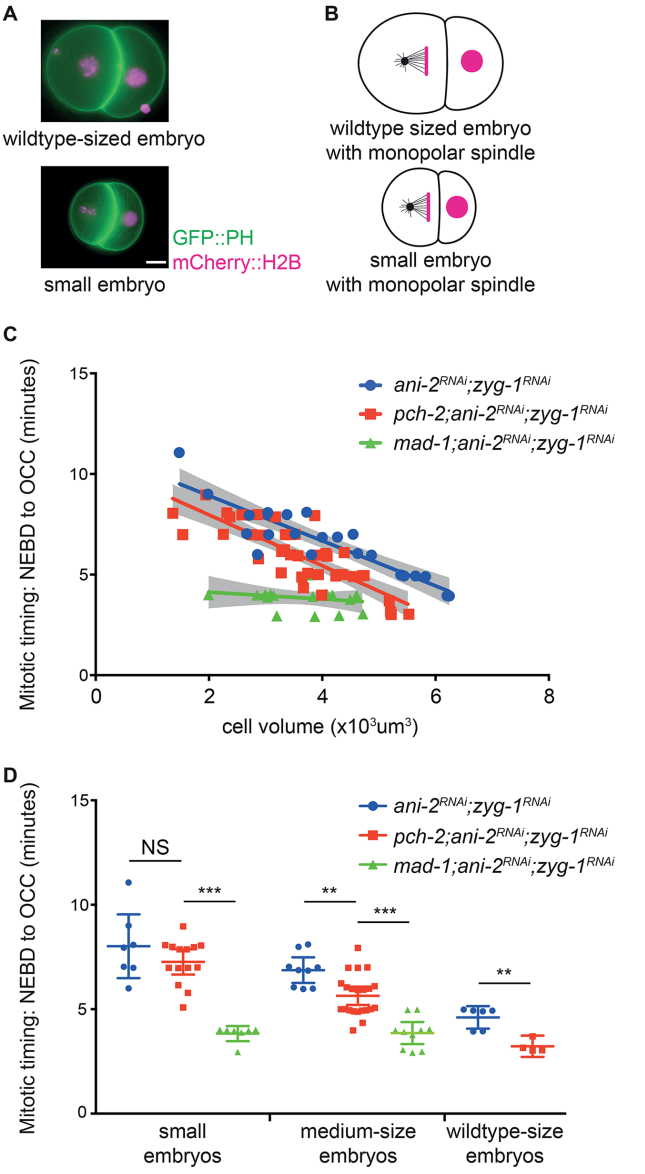


FIGURE 1: PCH-2 becomes dispensable for the spindle checkpoint response in somatic cells experimentally reduced in size. (A) Images of wild type–sized and small *ani-2$^{RNAi}$* two-cell embryos. Scale bar indicates 5 µm. (B) Cartoon of wild type–sized and small *ani-2$^{RNAi}$* two-cell embryos treated with *zyg-1$^{RNAi}$*. (C) Mitotic timing, as measured from nuclear envelope breakdown (NEBD) to the onset of cortical contractility (OCC), in AB cells of control and of *pch-2* and *mad-1* mutant embryos plotted against cell volume. Lines represent least-squares regression models with 95% confidence intervals (gray-shaded areas) for each set of data. Equations and *p* values indicating whether slopes are significantly nonzero for each model are as follows: *ani-2$^{RNAi}$;zyg-1$^{RNAi}$* (blue): $y = -1.117x + 11.15$ and $p < 0.0001$; *pch-2;ani-2$^{RNAi}$;zyg-1$^{RNAi}$* (red): $y = -1.264x + 10.50$ and $p < 0.0001$; *mad-1;ani-2$^{RNAi}$;zyg-1$^{RNAi}$* (green): $y = -0.1709x + 4.468$ and $p = 0.4197$. (D) Data from (C) partitioned into three categories: wild type–sized embryos (more than $5 \times 10^3$ µm$^3$), medium-sized embryos (between $3.3 \times 10^3$ and $5 \times 10^3$ µm$^3$), and small embryos (less than $3.3 \times 10^3$ µm$^3$). Error bars are 95% confidence intervals. In all graphs, a * indicates $p < 0.05$, ** indicates $p < 0.01$, and *** indicates $p < 0.0001$.

are consistent with what we have reported previously and report here for *zyg-1$^{RNAi}$* and *pch-2;zyg-1$^{RNAi}$* AB cells (Nelson *et al.*, 2015 and Supplemental Figure S4). The remaining cells, which ranged

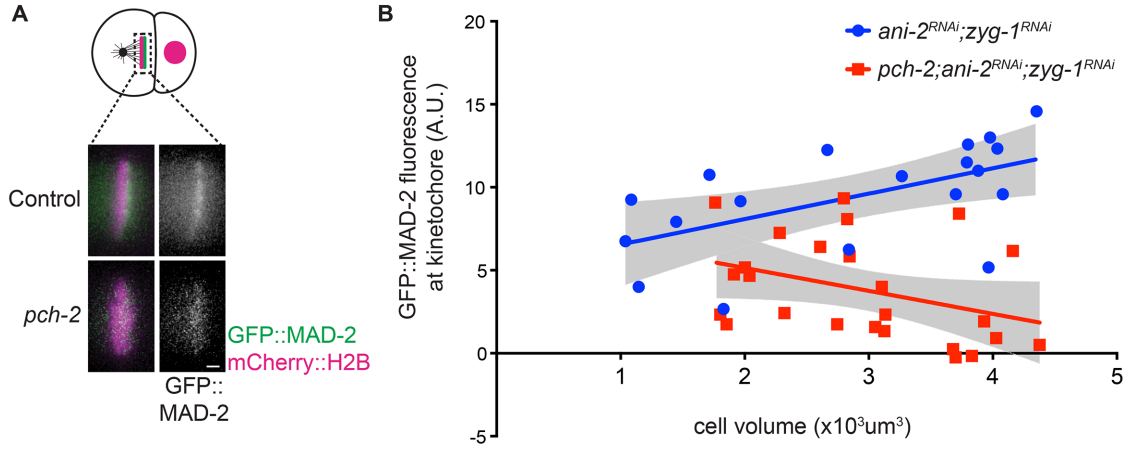


FIGURE 2: MAD-2 recruitment is partially restored to unattached kinetochores in *pch-2* mutant somatic cells experimentally reduced in size. (A) Cartoon and images of GFP::MAD-2 recruitment to unattached kinetochores in AB cells of control and *pch-2* AB cells treated with *ani-2* and *zyg-1* RNAi. Scale bar indicates 1 µm. (B) Quantification of kinetochore-bound GFP::MAD-2 in control and *pch-2* AB cells plotted against cell volume. Lines represent least-squares regression models with 95% confidence intervals (gray-shaded areas) for each set of data. Equations and *p* values indicating whether slopes are significantly nonzero for each model are as follows: *ani-2*$^{RNAi}$*;zyg-1*$^{RNAi}$ (blue): $y = 1.531x + 5.024$ and $p = 0.0115$; *pch-2;ani-2*$^{RNAi}$*;zyg-1*$^{RNAi}$ (red): $y = -1.384x + 7.911$ and $p = 0.0384$.

from $1.5 \times 10^3$ to $5 \times 10^3$ µm$^3$, were partitioned equally into two classes: medium-sized embryos were between $3.3 \times 10^3$ and $5 \times 10^3$ µm$^3$ and small embryos were between $1.5 \times 10^3$ and $3.3 \times 10^3$ µm$^3$. When embryos were partitioned into these two classes, medium-sized cells in *pch-2* mutants produced a checkpoint response intermediate between similarly sized control and *mad-1* mutant cells, while small *pch-2* cells had a robust checkpoint when compared with control and *mad-1* mutant cells (Figure 1D).

We verified that the mitotic delay observed in *pch-2* AB cells was a legitimate spindle checkpoint response by monitoring mitotic timing after performing double depletion of *ani-2* and *zyg-1* in *san-1* and *pch-2;san-1* mutant embryos. SAN-1 is the *C. elegans* ortholog of the essential spindle checkpoint factor Mad3 (Nystul *et al.*, 2003; Supplemental Figure S1B). There was no significant difference between the slopes of the regression analyses of *san-1* and *pch-2;san-1* data ($p = 0.8813$), and the slopes of the models were not statistically different than zero (Supplemental Figure S1B). However, we observed a slight increase in the length of the cell cycle as cells got smaller in *san-1* mutants, potentially reflecting that the spindle checkpoint in *C. elegans* is composed of two independent branches (Essex *et al.*, 2009). Altogether, these data allow us to draw two important conclusions. First, the requirement for PCH-2 during spindle checkpoint activation is proportional to cell volume in AB cells with monopolar spindles. And second, since we observe mitotic timing in small *pch-2* mutant AB cells similar to that in small control cells (Figure 1D), PCH-2 does not appear to affect spindle checkpoint silencing in *C. elegans*.

## MAD-2 recruitment is partially restored to unattached kinetochores in *pch-2* somatic cells experimentally reduced in size

We showed that PCH-2 is required for robust recruitment of Mad2 at unattached kinetochores during spindle checkpoint activation in AB cells of two-cell embryos (Nelson *et al.*, 2015). Therefore, we tested whether the checkpoint-induced delay we observed in small *pch-2;ani-2*$^{RNAi}$*;zyg-1*$^{RNAi}$ AB cells was accompanied by increased recruitment of GFP::MAD-2 at unattached kinetochores. We quantified GFP::MAD-2 recruitment at unattached kinetochores in pseudo-metaphase in control animals and *pch-2* mutants treated with *ani-2* and *zyg-1* RNAi (Figure 2A) and plotted GFP::MAD-2 fluorescence against cell volume (Figure 2B). Surprisingly, the regression analysis for control AB cells had a positive slope, suggesting that less GFP::MAD-2 at unattached kinetochores is required for spindle checkpoint function as these cells became smaller (Figure 2B). This was despite similar levels of soluble GFP::MAD2 around mitotic chromosomes after NEBD in both genetic backgrounds (Supplemental Figure S2, A and B). We observed that the regression analysis of GFP::MAD-2 fluorescence at unattached kinetochores in *pch-2;ani-2*$^{RNAi}$*;zyg-1*$^{RNAi}$ AB cells exhibited a negative slope, showing improved GFP::MAD-2 recruitment to unattached kinetochores as cells got smaller. However, the amount of GFP::MAD-2 was typically lower in fluorescence intensity than *ani-2*$^{RNAi}$*;zyg-1*$^{RNAi}$ control cells (Figure 2B). Therefore, our experiments demonstrate that MAD-2 recruitment is partially restored to unattached kinetochores in *pch-2* mutant somatic cells experimentally reduced in size.

## MAD-2 dosage controls checkpoint strength

*C. elegans* meiotic nuclei in the germline exist in a syncytium and cellularize after completing meiotic prophase. Knockdown of *ani-2* affects this cellularization event, resulting in a loss of cytoplasmic volume after nuclei are fully formed (Maddox *et al.*, 2005). MAD-2 is localized to the nucleus and nuclear envelope in these oocytes (Bohr *et al.*, 2015; Lawrence *et al.*, 2015; Figure 3A). Because embryonic nuclear size is not affected by *ani-2* RNAi (Supplemental Figure S3), we reasoned that as cells are genetically manipulated to decrease in cell volume, the absolute amount of Mad2 protein is likely to remain constant but its concentration to increase. Given that TRIP13 function is dispensable for checkpoint activation when O-Mad2 is readily available in human cells (Ma and Poon, 2018), we reasoned that something similar might be happening in *C. elegans* embryos. Specifically, we hypothesized that an increase in the concentration of Mad2, and O-Mad2 in particular, may explain the reduced requirement for PCH-2 in *ani-2*$^{RNAi}$*;zyg-1*$^{RNAi}$ small AB cells (Figure 3B).

To test this possibility, we initially attempted to visualize O-Mad2 directly in *C. elegans* embryos. Unfortunately, we were unable to

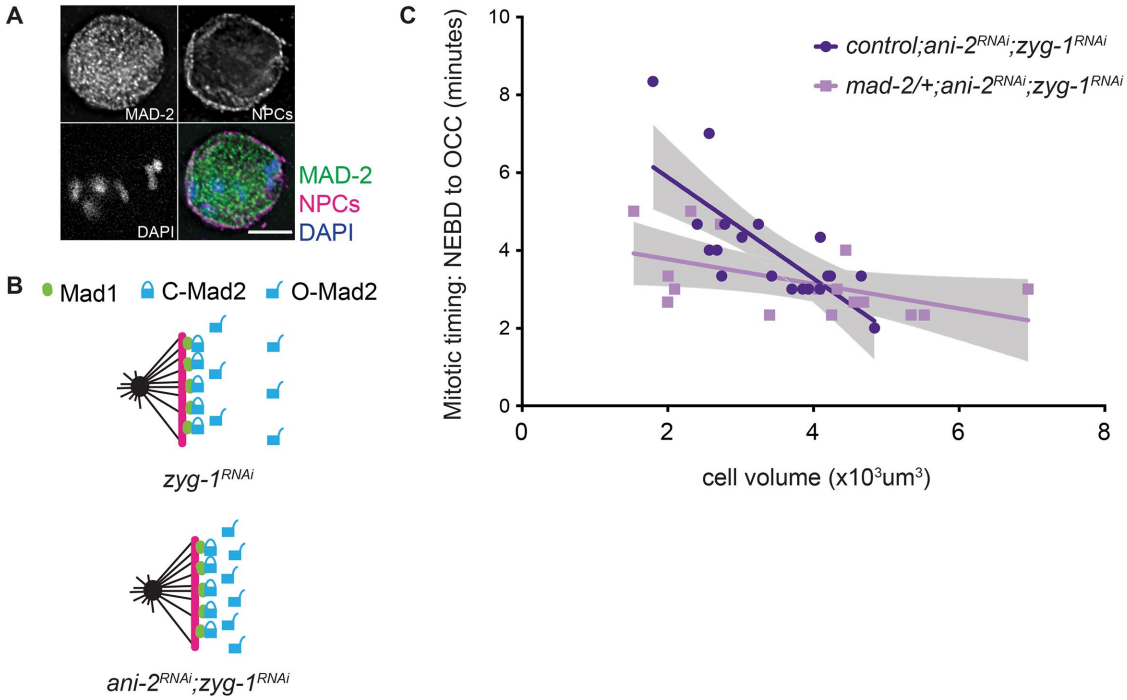


FIGURE 3: MAD-2 dosage controls checkpoint strength. (A) Immunostaining of MAD-2 and nuclear pore complex components (NPCs) shows MAD-2 localized in the nucleus and at the nuclear envelope during interphase. Scale bar indicates 5 µm. (B) Model depicting how a decrease in cell volume might result in an increase in the local concentration of O-Mad2 in *ani-2*$^{RNAi}$;*zyg-1*$^{RNAi}$ embryos, in contrast to *zyg-1*$^{RNAi}$ embryos. (C) Mitotic timing, as measured from nuclear envelope breakdown (NEBD) to the onset of cortical contractility (OCC), in AB cells of control and *mad-2/+* mutant embryos plotted against cell volume. Lines represent least-squares regression models with 95% confidence intervals (gray-shaded areas) for each set of data. Equations and *p* values indicating whether slopes are significantly nonzero for each model are as follows: control (dark purple): $y = -1.302x + 8.477$ and $p = 0.0002$; *mad-2/+* (light purple): $y = -0.3171x + 4.402$ and $p = 0.0395$.

perform this experiment with a commercial antibody (unpublished data). Further, we could not directly probe total Mad2 concentration as cells decreased in volume upon treatment with *ani-2* RNAi because GFP::MAD-2 did not localize to the nucleus and instead localized in the cytoplasm until NEBD (Essex *et al.*, 2009; Nelson *et al.*, 2015), making it an inaccurate reporter for this assay. Instead, we tested whether reducing Mad2 dosage affected checkpoint strength. We hypothesized that if Mad2 concentration influences checkpoint strength, reducing it by half should attenuate checkpoint strength in comparison to that in control animals. We performed double depletion of *ani-2* and *zyg-1* by RNAi in *mad-2* heterozygotes. Indeed, *mad-2* heterozygotes exhibited stronger spindle checkpoint strength as cells became smaller. However, the increase in spindle checkpoint strength was less robust than in control cells (Figure 3C). The slopes of the linear regressions for both control and *mad-2* heterozygotes were significantly nonzero, in contrast to similar experiments with *mad-1* and *san-1* homozygotes (Figure 1B and Supplemental Figure S1D). Therefore, spindle checkpoint strength depends on MAD-2 dosage.

We wondered whether the decrease in Mad2 protein levels might restore the reliance on PCH-2 in small embryos. However, *pch-2;mad-2/+* double mutants exhibited a substantial decrease in the production and viability of embryos, preventing us from performing these experiments: *pch-2;mad-2/+* double mutants produced broods that were 14% of control animals, and only 1% of these embryos were viable. Further, *pch-2;mad-2* double mutants could not be recovered from *pch-2;mad-2/+* mothers, a genetic interaction that we did not observe when we generated *pch-2;mad-1* double mutants (Bohr *et al.*, 2015) or *pch-2;san-1* double mutants (Supplemental Figure S1B). Worms with mutations in some spindle checkpoint mutants often display defects in fertility, viability, and development (Kitagawa and Rose, 1999; Stein *et al.*, 2007; Lara-Gonzalez *et al.*, 2019). Thus, in addition to MAD-2 dosage controlling checkpoint strength, it collaborates with PCH-2 to promote *C. elegans* fertility and viability.

## PCH-2 affects spindle checkpoint strength during embryogenesis

During embryogenesis, cell volume decreases and spindle checkpoint strength increases (Galli and Morgan, 2016; Gerhold *et al.*, 2018). Given that the requirement for PCH-2 is proportional to cell volume in two-cell embryos treated with *ani-2* RNAi, we assessed the role of PCH-2 in spindle checkpoint activation as cells decreased in size during normal embryogenesis.

We initially performed these experiments in embryos treated with nocodazole, which depolymerizes microtubules and induces spindle checkpoint activation in a manner similar to that when cells have monopolar spindles (Galli and Morgan, 2016; Gerhold *et al.*, 2018). We permeabilized embryos by performing *perm-1* RNAi (Carvalho *et al.*, 2011) and treated these embryos with nocodazole. Because we could not reliably visualize OCC in these dividing embryos, we measured mitotic timing from NEBD to decondensation of chromosomes (DECON) in cells of the AB lineage. These cells in control embryos exhibited a longer mitotic delay in 16-cell than in four-cell embryos (Figure 4A), verifying that the spindle checkpoint increases in strength as cells decrease in volume during

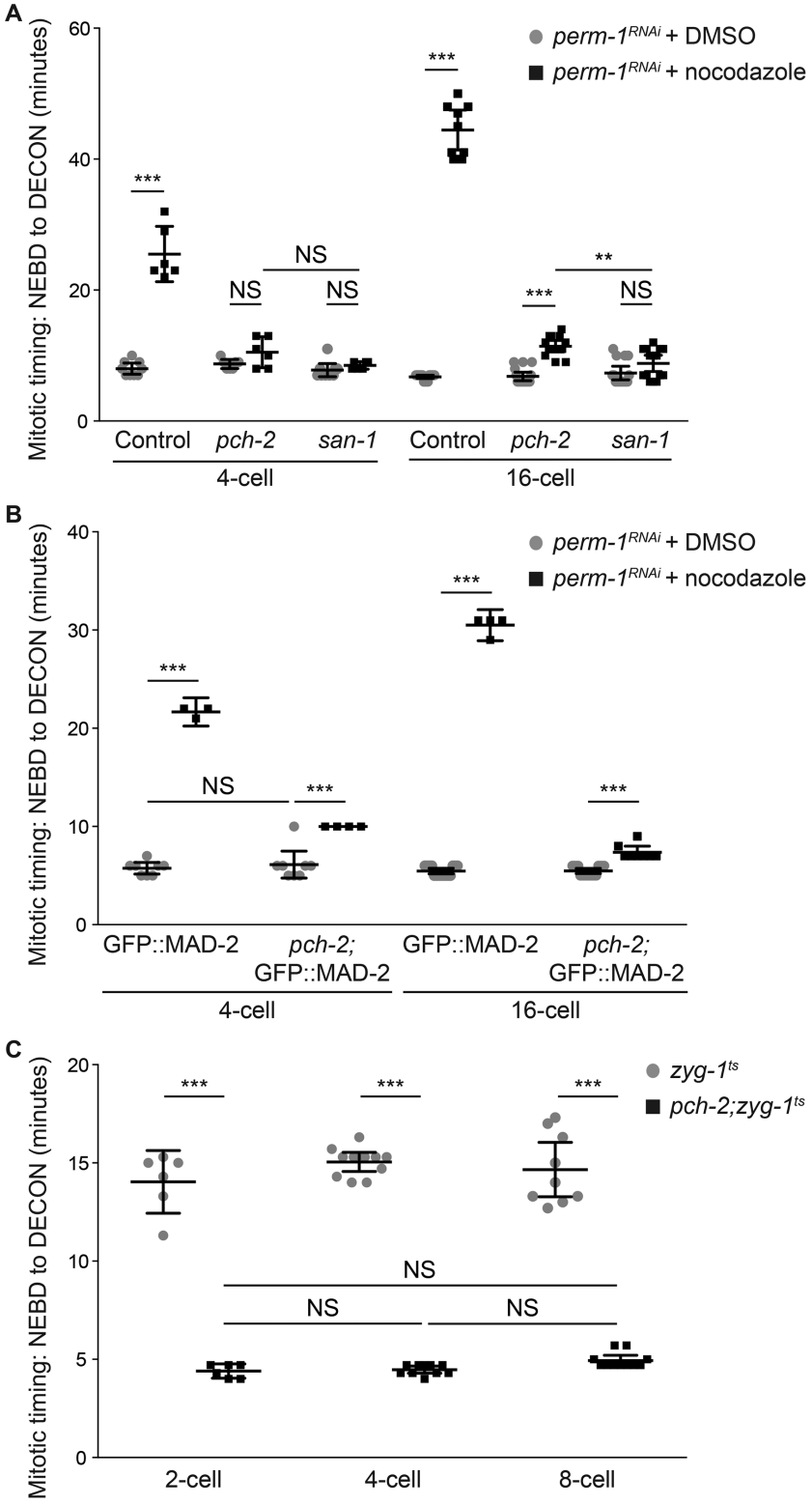


FIGURE 4: PCH-2 regulates spindle checkpoint strength during embryogenesis. (A) Mitotic timing, as measured from nuclear envelope breakdown (NEBD) to decondensation of chromatin (DECON), in control and *pch-2* and *san-1* mutant embryos treated with *perm-1* RNAi and DMSO or nocodazole at different developmental stages (4- and 16-cell embryos). (B) Mitotic timing in control and *pch-2* mutant embryos overexpressing GFP::MAD-2 and treated with *perm-1* RNAi and either DMSO or nocodazole at different developmental stages (4- and 16-cell embryos). (C) Mitotic timing in *zyg-1*$^{ts}$ and *pch-2;zyg-1*$^{ts}$ mutant embryos at different developmental stages (2-, 4-, and 8-cell embryos). All error bars are 95% confidence intervals.

embryogenesis (Galli and Morgan, 2016; Gerhold *et al.*, 2018). As a control, we performed the same experiment in *san-1* mutants and did not detect a mitotic delay when these embryos were treated with nocodazole (Figure 4A). Cells in four-cell *pch-2* mutant embryos treated with nocodazole showed greater variability in cell cycle timing than *san-1* mutants, but the average was not significantly different (Figure 4A). However, cells in the AB lineage in 16-cell *pch-2* mutant embryos treated with nocodazole exhibited a slight but significant cell cycle delay compared with similar cells in *pch-2* mutants treated with DMSO and *san-1* mutants treated with nocodazole. Thus, as cells of the AB lineage naturally decrease in cell size to 16-cell embryos, *pch-2* mutants treated with nocodazole exhibit some delay in the cell cycle, albeit not as prolonged as in control embryos, consistent with a defect in spindle checkpoint strength.

Given our hypothesis that Mad2 dosage might contribute to spindle checkpoint strength, particularly in *pch-2* mutants, we tested if a subtle increase in MAD-2 protein levels would suppress the defect in spindle checkpoint function or strength in *pch-2* mutant embryos. The presence of a GFP::MAD-2 transgene, in addition to endogenous MAD-2, results in about 2.5 times more MAD-2 in worms. This slight overexpression generates a normal spindle checkpoint response in control AB cells and can bypass the requirement for checkpoint components MAD-3 or BUB-3 (Essex *et al.*, 2009), but not PCH-2 (Nelson *et al.*, 2015), in AB cells of two-cell embryos with monopolar spindles. Overexpression of MAD-2 did not affect the checkpoint response in 16-cell *pch-2* embryos (Figure 4B). However, in contrast to our results in four-cell *pch-2* mutant embryos treated with nocodazole (Figure 4A), we found that overexpression of MAD-2 in cells of the AB lineage of four-cell *pch-2* embryos produced cell cycle delays compared with the same cells in embryos treated with DMSO. Again, these delays were not as dramatic as in control cells overexpressing GFP::MAD-2 (Figure 4B) but were significant, allowing us to conclude that slight overexpression of Mad2 partially restores checkpoint function to *pch-2* mutants as cells of the AB lineage decrease in size during embryogenesis, at least in four-cell embryos.

Given that we activated the spindle checkpoint in *ani-2*$^{RNAi}$ embryos by generating monopolar spindles (Figures 1C and 3C), we also formally tested whether *pch-2* mutant embryos with monopolar spindles exhibited defects in checkpoint strength, particularly in very early embryogenesis. We used a fast-acting temperature-sensitive allele of *zyg-1* (*zyg-1*$^{ts}$) (O'Rourke *et al.*, 2011) to activate the spindle checkpoint in developing embryos with two, four, and eight cells. We shifted embryos at different stages of development, verified the appearance of monopolar

spindles, and measured mitotic timing from NEBD to DECON. In control *zyg-1*$^{ts}$ mutant embryos, we observed a delay in mitotic timing in cells from the AB lineage ,and this delay became only marginally longer as embryos had more cells (Figure 4C), similarly to previous reports (Gerhold *et al.*, 2018). In stark contrast to our *ani-2*$^{RNAi}$ experiments, the mitotic timing observed in *pch-2;zyg-1*$^{ts}$ mutant embryos was the same in AB cells of two-, four-, and eight-cell embryos and significantly reduced in comparison to *zyg-1*$^{ts}$ embryos. Thus, similar to our results with four-cell *pch-2* mutant embryos treated with nocodazole, *pch-2* mutants exhibit no cell cycle delay in the presence of monopolar spindles in AB cells in two-, four-, and eight-cell embryos. However, additional considerations may make direct comparisons between our *ani-2*$^{RNAi}$*;zyg-1*$^{RNAi}$ experiments and *zyg-1*$^{ts}$ embryos difficult (see *Discussion*).

### PCH-2 is responsible for the stronger spindle checkpoint in the germline lineage

Cell fate is another important determinant of spindle checkpoint strength. In *C. elegans* embryos, the spindle checkpoint is stronger in germline precursor cells than in similarly sized somatic counterparts (Galli and Morgan, 2016; Gerhold *et al.*, 2018). However, as we observed with AB cells (Nelson *et al.*, 2015), PCH-2 is essential for the spindle checkpoint in wild type–sized $P_1$ cells (Supplemental Figure S4). Therefore, having established that PCH-2 becomes dispensable for the spindle checkpoint as two-cell embryos are genetically manipulated to become smaller (Figure 1, C and D), we tested whether PCH-2 contributed to the stronger spindle checkpoint in $P_1$ cells of two-cell embryos treated with *ani-2* RNAi (Figure 5 and Supplemental Figure S4B). Consistent with other reports (Galli and Morgan, 2016; Gerhold *et al.*, 2018), when we performed double depletion of *ani-2* and *zyg-1* in control embryos and monitored mitotic timing, we observed $P_1$ cells with volumes similar to those of AB cells exhibiting a longer cell cycle delay (Figure 5A and Supplemental Figure S4B; Supplemental Videos 5 and 6). Further, the regression analysis that best fit control $P_1$ data is significantly different and steeper than that of control AB cells ($p < 0.0001$), indicating that variables in addition to cell volume contribute to the spindle checkpoint strength in germline precursor cells. When we knocked down both *ani-2* and *zyg-1* in *pch-2* mutant embryos, we no longer observed a significant difference ($p = 0.9096$) between the slopes of the regression analysis of $P_1$ and AB cells (Figure 5B and Supplemental Figure S4B; Supplemental Videos 7 and 8), indicating that PCH-2 is responsible for the stronger checkpoint in $P_1$ cells.

We observed that cell cycle timing was faster in *pch-2* mutant $P_1$ cells than similarly sized *pch-2* mutant AB cells after treatment with *ani-2* and *zyg-1* RNAi (Figure 5B and Supplemental Figure S4B). We wondered if embryonic germline precursor cells might rely on some spindle checkpoint proteins for normal mitotic timing, analogously to mitotically dividing stem cells in the *C. elegans* germline (Gerhold *et al.*, 2015) and similarly to mammalian cultured cells (Meraldi *et al.*, 2004; Rodriguez-Bravo *et al.*, 2014; Ma and Poon, 2016). To address this, we measured normal mitotic timing in AB and $P_1$ cells of both control and *pch-2* mutant embryos. We found that while normal mitotic timing is unaffected by mutation of *pch-2* in AB cells, *pch-2* mutant $P_1$ cells go through mitosis significantly faster than control $P_1$ cells (Figure 5C), thus providing an explanation for the faster cell cycle timing in *pch-2* mutant $P_1$ cells with the same cell volume as *pch-2* mutant AB cells after treatment with *ani-2* and *zyg-1* RNAi. We saw a decrease in the cell cycle timing of $P_1$ cells in *mad-1* mutants but this was not significantly different than control $P_1$ cells (Figure 5C).

### PCH-2′s enrichment in $P_1$ cells depends on PAR-1 and PAR-6

Cell fate is driven by the asymmetric distribution of various determinants between somatic and germline lineages during early divisions of the *C. elegans* embryo (Rose and Gonczy, 2014). Because we found that PCH-2 promoted the spindle checkpoint strength in both AB and $P_1$ cells, but even more dramatically in $P_1$ cells, we asked if PCH-2 was regulated differently between these cells. First, we tested whether PCH-2::GFP could also support the stronger checkpoint in $P_1$ cells. We treated embryos expressing PCH-2::GFP with *zyg-1* RNAi and evaluated mitotic timing in both AB and $P_1$ cells, using chromosome decondensation as a marker for mitotic exit. $P_1$ cells expressing PCH-2::GFP had full checkpoint function, exhibiting a mitotic delay longer than that in AB cells also expressing PCH-2::GFP and not significantly different from that in control $P_1$ cells treated with *zyg-1* RNAi (Figure 6A).

Previous transcriptome analysis of PCH-2 did not reveal asymmetric enrichment of PCH-2 mRNA between AB and $P_1$ cells (Tintori *et al.*, 2016). We tested whether PCH-2::GFP exhibited differences in protein levels between AB and $P_1$ cells. First, we assessed whether PCH-2::GFP was more enriched in pseudo-metaphase at unattached kinetochores in $P_1$ than AB cells. We quantified PCH-2::GFP fluorescence at unattached kinetochores in both AB and $P_1$ cells of embryos treated with *zyg-1* RNAi but did not detect any difference between the two cell types (Supplemental Figure S5, A and B). Similarly, we did not detect any difference in GFP::MAD-2 recruitment at unattached kinetochores between AB and $P_1$ cells in *zyg-1*$^{RNAi}$ embryos (Supplemental Figure S5, C and D).

Checkpoint factors, including MAD-2 and PCH-2, form a diffuse "cloud" around mitotic chromosomes after NEBD, even during normal cell cycles (Essex *et al.*, 2009; Nelson *et al.*, 2015). We wondered if PCH-2::GFP fluorescence in this cloud might be different between AB and $P_1$ cells. First, we verified that PCH-2::GFP fluorescence around mitotic chromosomes was similar between AB cells during unperturbed (control) or monopolar mitosis (*zyg-1*$^{RNAi}$; Supplemental Figure S6). PCH-2::GFP fluorescence around chromosomes was significantly higher in *zyg-1*$^{RNAi}$ AB cells than in control AB cells (Supplemental Figure S6B). However, we noticed that the area occupied by PCH-2::GFP in control AB cells was significantly larger than that of *zyg-1*$^{RNAi}$ AB cells (yellow dashed circle in Supplemental Figure S6A and quantified in Supplemental Figure S6C). When we factored this larger area of PCH-2::GFP fluorescence into our analysis, we observed a similar amount of PCH-2::GFP around mitotic chromosomes in both control and *zyg-1*$^{RNAi}$ AB cells (Supplemental Figure S6D).

Having established that AB cells had similar amounts of PCH-2::GFP whether the checkpoint was active or not, we quantified PCH-2::GFP fluorescence in the area around mitotic chromosomes in AB and $P_1$ cells during unperturbed cell cycles. Similarly to AB cells (Nelson *et al.*, 2015 and Supplemental Figure S6A), we observed PCH-2::GFP enriched in the area around the chromosomes in prometaphase in $P_1$ cells (Figure 6B). When we quantified the fluorescence of PCH-2::GFP in this area surrounding chromosomes after NEBD in both AB and $P_1$ cells, we detected a statistically significant enrichment of PCH-2::GFP in the area surrounding chromosomes in $P_1$ cells (Figure 6C) but not in the cytoplasm of $P_1$ cells (Supplemental Figure S7, A and B). Although this enrichment is limited to a "cloud" around mitotic chromosomes (see Supplemental Figure S7B), we verified that this enrichment was not the indirect consequence of the smaller volume of $P_1$ cells by quantifying PCH-2::GFP fluorescence in *gpr-1/2*$^{RNAi}$ embryos. This double knockdown equalizes the size of AB and $P_1$ cells without affecting their cell fate (Colombo *et al.*, 2003; Gotta *et al.*, 2003;

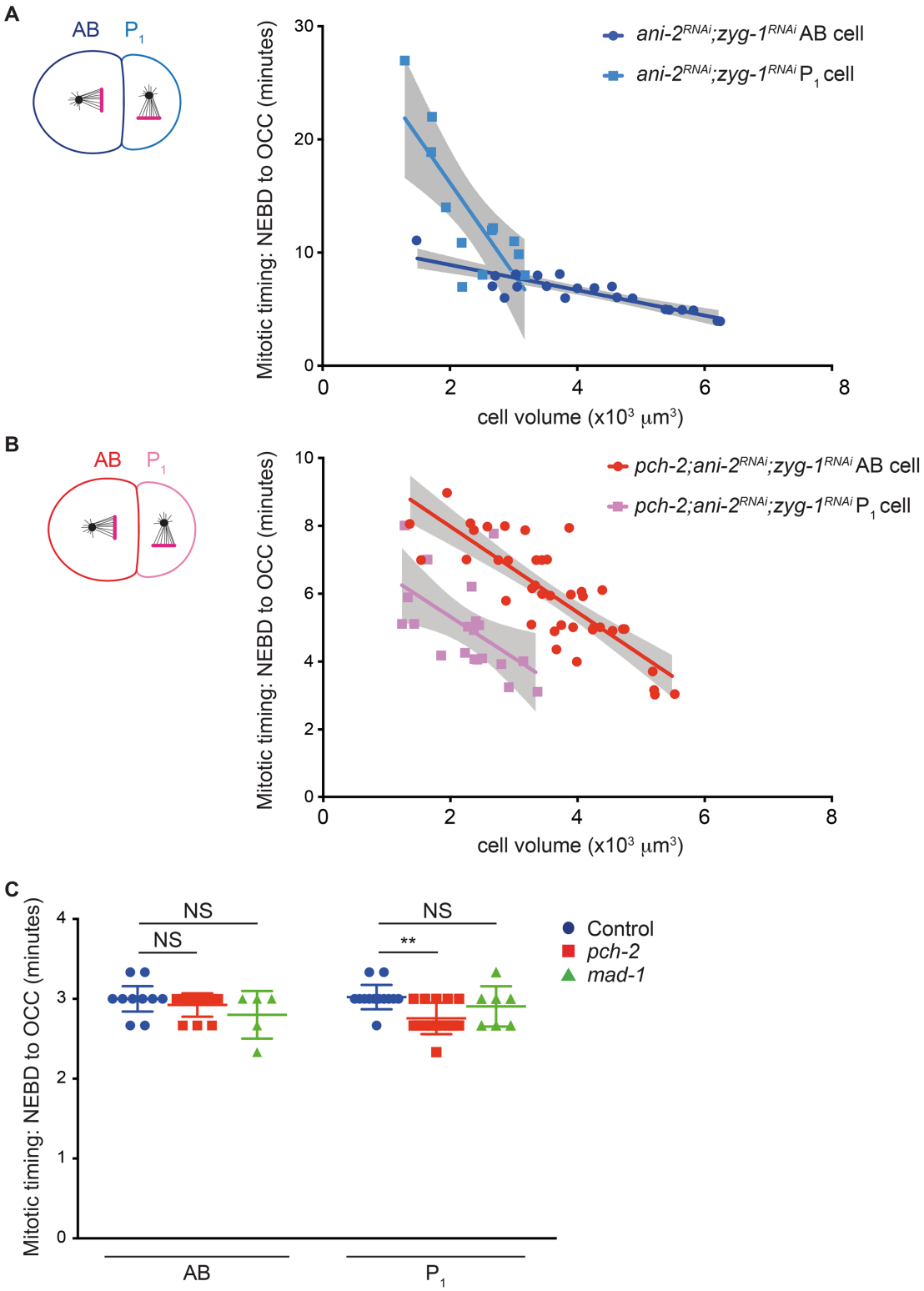


FIGURE 5: PCH-2 is responsible for the stronger spindle checkpoint in the germline lineage. Mitotic timing, as measured from nuclear envelope breakdown (NEBD) to the onset of cortical contractility (OCC), in AB and $P_1$ cells plotted against cell volume in control *ani-2*$^{RNAi}$;*zyg-1*$^{RNAi}$ embryos (A) or *pch-2*;*ani-2*$^{RNAi}$;*zyg-1*$^{RNAi}$ (B) embryos. Lines represent least-squares regression models with 95% confidence intervals (gray-shaded areas) for each set of data. Equations and *p* values indicating whether slopes are significantly nonzero for each model are as follows: *ani-2*$^{RNAi}$;*zyg-1*$^{RNAi}$ AB (dark blue): $y = -1.117x + 11.15$ and $p < 0.0001$; *ani-2*$^{RNAi}$;*zyg-1*$^{RNAi}$ $P_1$ (light blue): $y = -8.047x + 32.27$ and $p = 0.0021$; *pch-2*;*ani-2*$^{RNAi}$;*zyg-1*$^{RNAi}$ AB (red): $y = -1.264x + 10.50$ and $p < 0.0001$; *pch-2*;*ani-2*$^{RNAi}$;*zyg-1*$^{RNAi}$ $P_1$ (pink): $y = -1.218x + 7.75$ and $p = 0.0125$. Data for AB cells in both control and *pch-2* mutants are the same as in Figure 1C. (C) Mitotic timing of AB and $P_1$ cells in controls and in *pch-2* and *mad-1* mutants during unperturbed divisions. Error bars are 95% confidence intervals.

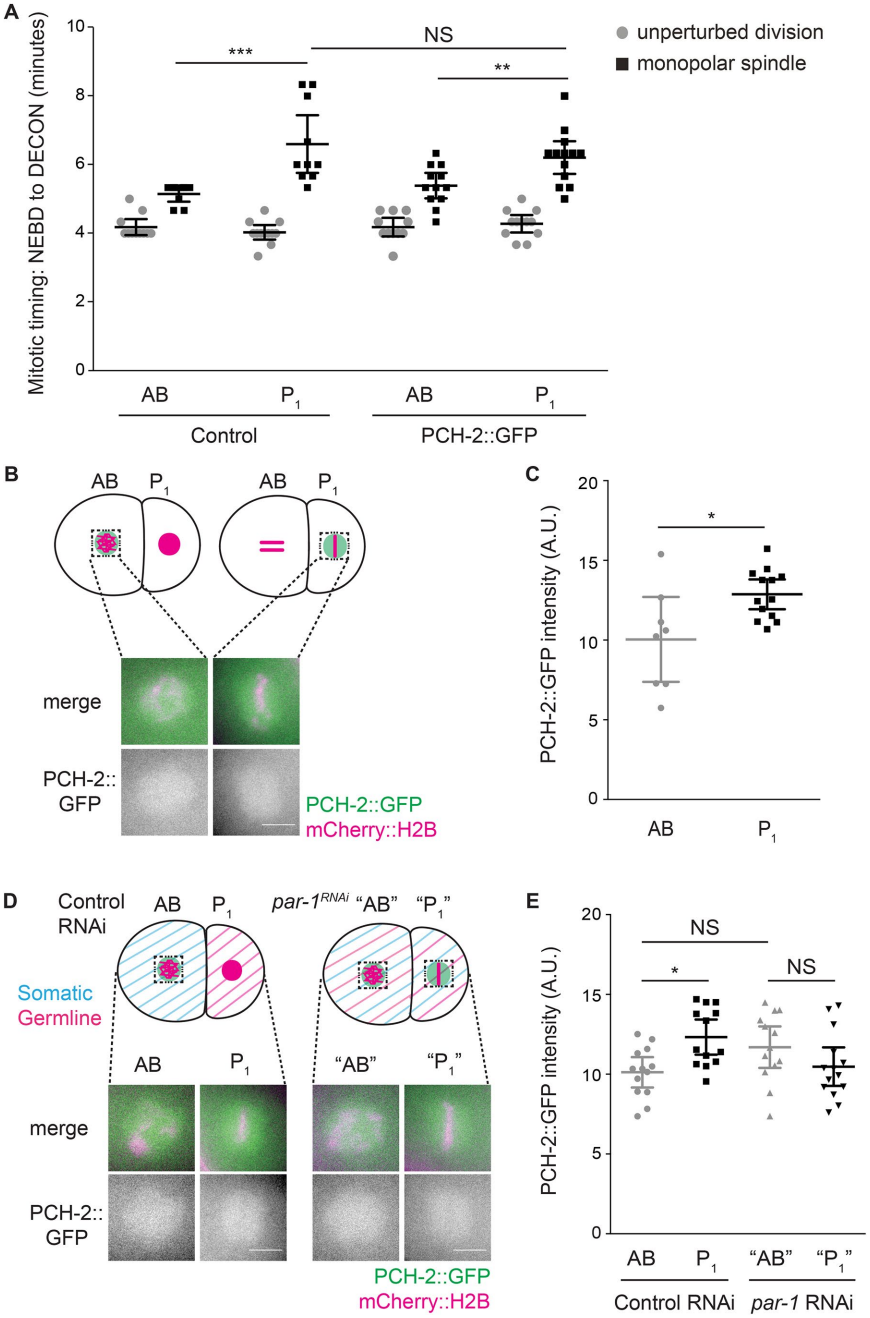


**FIGURE 6:** PCH-2's enrichment around mitotic chromosomes in $P_1$ cells depends on PAR-1. (A) Mitotic timing of control embryos and embryos expressing PCH-2::GFP during unperturbed divisions or in the presence of monopolar spindles. (B) Cartoon and images of PCH-2::GFP localization around mitotic chromosomes in AB and $P_1$ cells of two-cell embryos. Scale bar indicates 5 µm. (C) Quantification of PCH-2::GFP fluorescence in AB and $P_1$ cells. (D) Cartoon and images of PCH-2::GFP localization around mitotic chromosomes in AB and $P_1$ cells of control RNAi and *par-1*$^{RNAi}$ two-cell embryos. (E) Quantification of PCH-2::GFP fluorescence in AB and $P_1$ cells of *par-1*$^{RNAi}$ embryos. All error bars are 95% confidence intervals. NS indicates not significant.

Srinivasan *et al.*, 2003). RNAi of *gpr-1/2* showed variability in the effect on AB and $P_1$ cell size (Supplemental Figure S7C). However, when we limited our analysis of PCH-2::GFP fluorescence to embryos in which AB and $P_1$ cells were of similar area (red symbols in Supplemental Figure S7C), we observed an enrichment of PCH-2::GFP in $P_1$ cells similar to that in control embryos (Supplemental Figure S7, D and E).

To better understand the relationship between PCH-2 enrichment in $P_1$ cells and cell fate, we abrogated the asymmetry of the two-cell embryo by performing RNAi against the essential polarity factors, PAR-1 (Guo and Kemphues, 1995) and PAR-6 (Hung and Kemphues, 1999). These factors antagonize each other, with PAR-6 at the anterior cortex and PAR-1 at the posterior cortex of early embryos, to establish asymmetries during the first two embryonic divisions (Goldstein and Macara, 2007). In *par-1*$^{RNAi}$ and *par-6*$^{RNAi}$ mutant embryos, AB and $P_1$ cells exhibit similar checkpoint strength (Gerhold *et al.*, 2018), indicating that the stronger spindle checkpoint response in $P_1$ cells depends on this asymmetric division. Despite the loss of cell fate in *par-1*$^{RNAi}$ and *par-6*$^{RNAi}$ embryos, we will refer to the anterior blastomere as "AB" and the posterior as "$P_1$." We verified the efficiency of *par-1* and *par-6* RNAi by measuring cell area and found that AB and $P_1$ cells approached similar sizes in both conditions (Supplemental Figure S8, A and B), although AB cells were still significantly larger than $P_1$ cells in *par-1*$^{RNAi}$ mutant embryos (Supplemental Figure S8A). We quantified PCH-2::GFP fluorescence in the area around chromosomes in AB and $P_1$ cells after *par-1* RNAi and observed that the fluorescence of PCH-2::GFP, despite being slightly lower in $P_1$ cells, was not significantly different between AB and $P_1$ cells, unlike what we observed in embryos exposed to control RNAi (Figure 6, D and E). AB and $P_1$ cells treated with *par-6* RNAi showed equal PCH-2::GFP fluorescence (Supplemental Figure S8, C and D). Therefore, PCH-2::GFP's enrichment around mitotic chromosomes in $P_1$ cells depends on the conserved factors that induce embryonic asymmetry and germline cell fate, PAR-1 and PAR-6.

## The stronger checkpoint in $P_1$ cells depends on CMT-1

In vitro, the *C. elegans* ortholog of p31$^{comet}$, CMT-1, is required for PCH-2 to bind and remodel Mad2 (Ye *et al.*, 2015). In addition to this role, CMT-1 is also needed to localize PCH-2 to unattached kinetochores and generate a robust spindle checkpoint response in AB cells (Nelson *et al.*, 2015). Therefore, we reasoned that CMT-1 might also be needed for the stronger checkpoint in $P_1$ cells.

To test this possibility, we first performed double knockdown of *ani-2* and *zyg-1* in *cmt-1* mutants and monitored the length of the spindle checkpoint response as AB and $P_1$ cells became smaller (Figure 7A; Supplemental Videos 9-12). When the results were compared with the regression model for control AB cells (opaque blue line in Figure 7A), we saw that *cmt-1* AB cells consistently exhibit a weaker checkpoint at all cell volumes. Similarly to *pch-2;ani-2*$^{RNAi}$*;zyg-1*$^{RNAi}$ mutants (Figure 5B), the stronger spindle checkpoint response in $P_1$ cells was lost in *cmt-1;ani-2*$^{RNAi}$*;zyg-1*$^{RNAi}$ mutants and we did not observe any statistical difference between

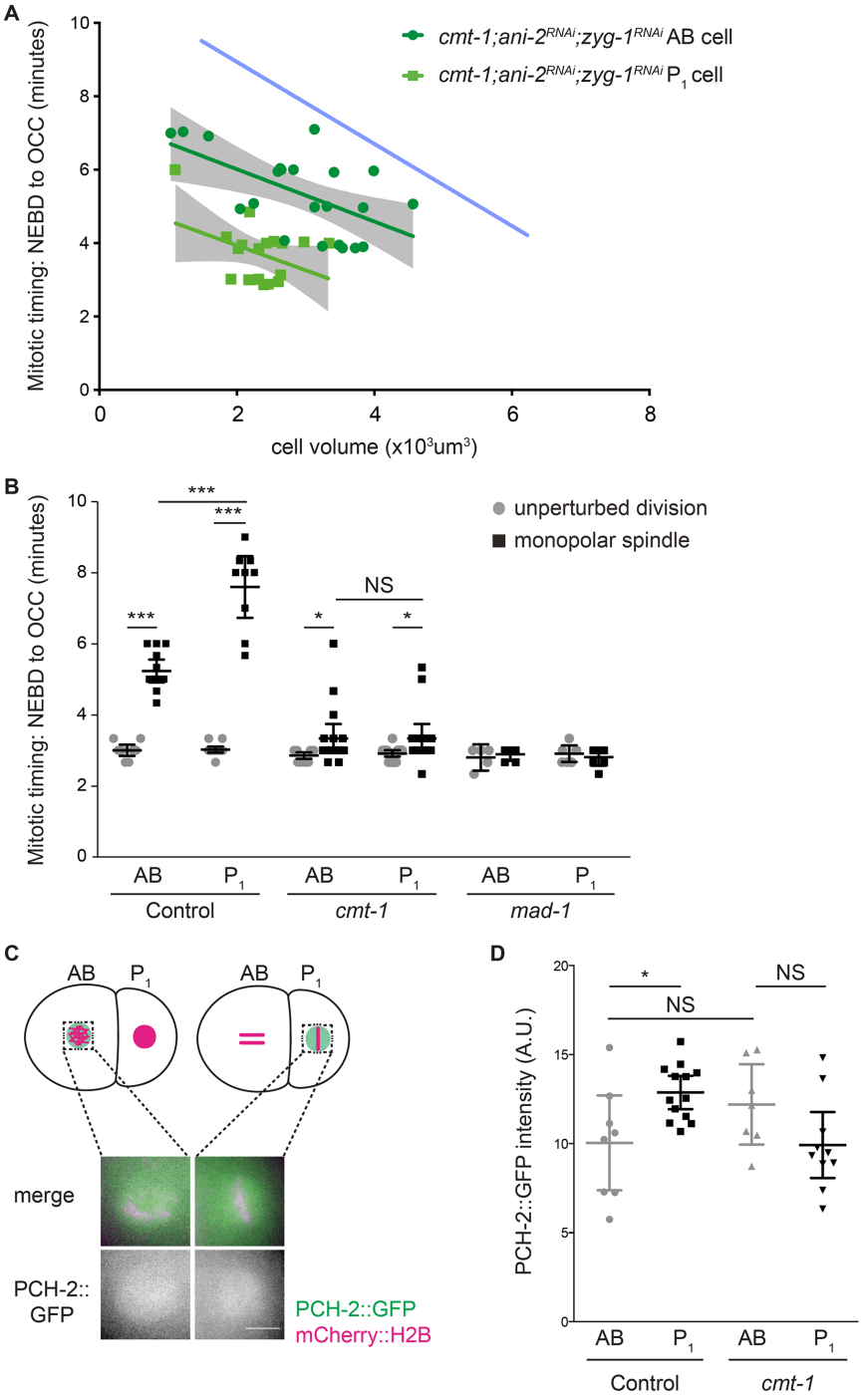


FIGURE 7: The stronger checkpoint in $P_1$ cells depends on CMT-1. (A) Mitotic timing, as measured from nuclear envelope breakdown (NEBD) to the onset of cortical contractility (OCC), in AB and $P_1$ cells plotted against cell volume in *cmt-1;ani-2*$^{RNAi}$*;zyg-1*$^{RNAi}$ embryos. Lines represent least-squares regression models with 95% confidence intervals (gray-shaded areas) for each set of data. The opaque blue line represents the regression model of the control AB data from Figure 1C. Equations and *p* values indicating whether slopes are significantly nonzero for each model are as follows: *cmt-1;ani-2*$^{RNAi}$*;zyg-1*$^{RNAi}$ AB (dark green): $y = -0.713x + 7.44$ and $p = 0.0050$; *cmt-1;ani-2*$^{RNAi}$*;zyg-1*$^{RNAi}$ $P_1$ (light green): $y = -0.6767x + 5.291$ and $p = 0.0452$. (B) Mitotic timing of control and *cmt-1* and *mad-1* mutant embryos during unperturbed divisions or in the presence of monopolar spindles. (C) Cartoon and images of PCH-2::GFP localization around mitotic chromosomes in AB and $P_1$ cells of *cmt-1* mutant embryos. Scale bar indicates 5 µm. (D) Quantification of PCH-2::GFP fluorescence in AB and $P_1$ cells of *cmt-1* mutant embryos. All error bars are 95% confidence intervals. NS indicates not significant.

the between the slopes of the regression analysis of $P_1$ and AB cells ($p = 0.9403$). We also observed that cell cycle timing was faster in *cmt-1* $P_1$ cells that were similar in volume to *cmt-1* AB cells (Figure 7A). Thus, CMT-1 is also essential to promote spindle checkpoint strength in germline precursor cells.

We also performed *zyg-1* RNAi on control and *cmt-1* mutant embryos and monitored mitotic timing in both AB and $P_1$ cells. AB and $P_1$ cells of control and *cmt-1* mutant embryos treated with control RNAi had similar mitotic timing. Unlike similar experiments in *pch-2* mutants (Figure 5C), we did not detect a statistically significant difference between cell cycle time in $P_1$ cells between wild-type and *cmt-1* mutant embryos (Figure 7B), suggesting that *ani-2*$^{RNAi}$*;zyg-1*$^{RNAi}$ embryos might be more sensitive to subtle perturbations in cell cycle timing. In *zyg-1*$^{RNAi}$ embryos, $P_1$ cells exhibited a stronger checkpoint response than AB cells (Figure 7B). In contrast, both AB and $P_1$ cells in *cmt-1;zyg-1*$^{RNAi}$ mutant embryos exhibited similar spindle checkpoint delays (Figure 7B). Despite having spindle checkpoint responses that were less robust than that of control *zyg-1*$^{RNAi}$ embryos, AB and $P_1$ cells in *cmt-1* mutant embryos treated with *zyg-1* RNAi spent significantly longer in mitosis than *cmt-1* mutant embryos treated with control RNAi (Figure 7B), indicating that they activated a weaker spindle checkpoint response, similar to our published results (Nelson *et al.*, 2015). More importantly, *cmt-1;zyg-1*$^{RNAi}$ mutant embryos failed to generate a stronger checkpoint in $P_1$ cells, consistent with *cmt-1;ani-2*$^{RNAi}$*;zyg-1*$^{RNAi}$ experiments (Figure 7A).

Aside from localizing PCH-2 to unattached kinetochores (Nelson *et al.*, 2015), we wondered if CMT-1 was required for any other aspects of PCH-2 regulation. Therefore, we tested whether CMT-1 was necessary for PCH-2's asymmetric enrichment in $P_1$ cells. We quantified PCH-2::GFP fluorescence in prometaphase in the area around chromosomes in both *cmt-1* mutant AB and $P_1$ cells (Figure 7C). First, we found that PCH-2::GFP fluorescence was slightly higher in AB cells in *cmt-1* mutants than in control embryos (Figure 7D). We saw a similar result in our *par-1* RNAi experiments, although in both cases these increases were not statistically significant. However, unlike the case with *par-1*$^{RNAi}$ embryos (Gerhold *et al.*, 2018), this increase in PCH-2::GFP was not accompanied by an increase in checkpoint strength (Figure 7B), consistent with our hypothesis that the weaker checkpoint in *cmt-1* AB cells is a consequence of PCH-2's absence from unattached kinetochores (Nelson *et al.*, 2015). Further, when we compared the quantification of PCH-2::GFP fluorescence in *cmt-1* mutant AB and $P_1$ cells (Figure 7C), we did not detect a significant difference between the two

types of cells (Figure 7D), unlike our experiment in control embryos (Figure 6, B and C), indicating that CMT-1 contributes to the asymmetric enrichment of PCH-2 in $P_1$ cells. Thus, CMT-1 promotes spindle checkpoint strength through two mechanisms: localizing PCH-2 to unattached kinetochores and ensuring its enrichment in germline precursor cells.

## DISCUSSION

The role of PCH-2, and its mammalian ortholog TRIP13, in the spindle checkpoint has been enigmatic (see Table 1). Originally identified as a checkpoint silencing factor (Eytan *et al.*, 2014; Wang *et al.*, 2014; Miniowitz-Shemtov *et al.*, 2015; Ye *et al.*, 2015; Brulotte *et al.*, 2017; Alfieri *et al.*, 2018), more recent evidence also indicates a role in promoting the checkpoint response (Nelson *et al.*, 2015; Ma and Poon, 2016, 2018; Yost *et al.*, 2017). It is clear that the reliance on PCH-2/TRIP13 in checkpoint activation reflects the relative levels and availability of O-Mad2 (Ma and Poon, 2018). We show here that PCH-2 also controls checkpoint strength. Surprisingly, we can uncouple PCH-2's requirement for checkpoint activation, which we detect in both AB and $P_1$ cells of wild type–sized two-cell embryos (Nelson *et al.*, 2015 and Supplemental Figure S4), from the requirement for spindle checkpoint strength, which we observe when we genetically manipulate the cell size of two-cell embryos by *ani-2* RNAi (Figures 1C and 5B). Based on this, we propose that PCH-2 regulates checkpoint strength not simply by regulating O-Mad2 availability, but by doing so specifically at and near unattached kinetochores, providing an unanticipated mechanism to explain this phenomenon (Figure 8). Given that *cmt-1* mutants exhibit decreased Mad2 protein levels (Nelson *et al.*, 2015), suggesting that CMT-1's binding to C-Mad2 stabilizes the protein in *C. elegans*, we speculate that PCH-2 is specifically disassembling a C-Mad2/CMT-1 complex to generate this pool of O-Mad2. This role in checkpoint strength appears to be particularly important in large cells, such as oocytes and cells in early embryos, as well as cells that give rise to immortal germ cells.

Our model assumes that two-cell embryos have a significant amount of O-Mad2 available, even when PCH-2 function is lost (Figure 8), unlike what is reported in human cells (Ma and Poon, 2016). Given that this is a developmental system in which embryos have undergone only a single mitotic division before we perform our assays and newly synthesized Mad2 adopts the open conformation (Kim *et al.*, 2018), we propose that O-Mad2 is not limiting in very early embryos, even in *pch-2* null mutants. In this way, *C. elegans* two-cell embryos would be analogous to human cells undergoing cell division soon after acute depletion of TRIP13 (Ma and Poon, 2018). Unfortunately, we were unable to directly probe O-Mad2 concentration or its availability at or near unattached kinetochores in small *ani-2*$^{RNAi}$ embryos or germline precursor cells. However, we think that several pieces of data support our model (Figure 8). PCH-2's characterized biochemical activity regulates the availability of O-Mad2 (Ye *et al.*, 2015; Brulotte *et al.*, 2017; Alfieri *et al.*, 2018), making this the likely mechanism through which PCH-2 regulates checkpoint strength. PCH-2 at unattached kinetochores in AB and $P_1$ cells (Nelson *et al.*, 2015 and Figure 7B) and its enrichment around mitotic chromosomes in $P_1$ cells (Figures 5A and 6C) correlates with a stronger checkpoint. The loss of PCH-2 or this enrichment produces similar checkpoint strength between AB and $P_1$ cells (Gerhold *et al.*, 2018, Figures 1C, 5B, 6E, and 7, A and D, and Supplemental Figure S7D). Indeed, the equalization of PCH-2::GFP between AB and $P_1$ cells that we observe in *par-1*$^{RNAi}$ and *par-6*$^{RNAi}$ embryos (Figure 6E and Supplemental Figure S8D) is entirely consistent with the observation that in these mutants, AB cells more closely resemble $P_1$ cells in spindle checkpoint strength (Gerhold *et al.*, 2018). Finally, checkpoint strength depends on Mad2 dosage (Figure 2C), particularly in AB cells of four-cell *pch-2* mutant embryos (Figure 4B).

Another prediction of our model is that overexpression of Mad2 should also make PCH-2 dispensable for spindle checkpoint activation. We've shown that subtle elevations of Mad2 protein levels introduce a cell cycle delay in AB cells of four-cell embryos treated with nocodazole but not those treated with DMSO (Figure 4B), entirely consistent with our model. However, it is not clear why we do not observe a similar effect in cells of the AB lineage of 16-cell embryos that overexpress Mad2 (Figure 4B). Unfortunately, more dramatic overexpression experiments are technically difficult in *C. elegans*. Further, it is likely that strong overexpression of Mad2 in *C. elegans* embryos will delay normal mitosis, consistent with similar findings in mammalian cells (Marks *et al.*, 2017) and budding yeast (Mariani *et al.*, 2012). In this way, PCH-2's function may

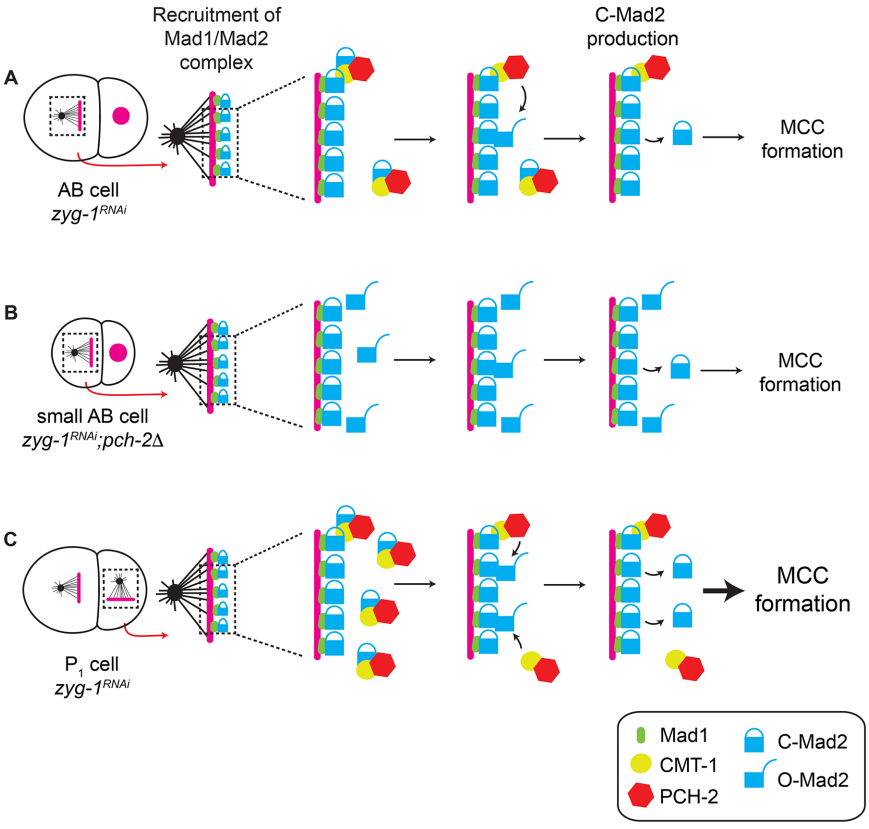


**FIGURE 8:** Model. (A) A robust spindle checkpoint response in large cells requires the presence of PCH-2 at unattached kinetochores to increase the local concentration of O-MAD-2 at and near unattached kinetochores. (B) Reducing cell volume of two-cell embryos increases the concentration of O-Mad-2 at and near unattached kinetochores, allowing a checkpoint response in the absence of PCH-2. (C) The enrichment of PCH-2 around mitotic chromosomes in $P_1$ cells results in a greater production of O-MAD-2, generating a stronger spindle checkpoint response in these cells.

provide a useful buffer: Because Mad2 protein levels may need to stay within a narrow range to allow normal mitotic timing, PCH-2's localization at and near unattached kinetochores provide a mechanism to increase O-Mad2's local concentration to promote effective and efficient signaling during checkpoint activation.

The requirement for PCH-2 in spindle checkpoint strength is also seen as AB cells normally decrease in volume during embryogenesis (Figure 4A), although not as dramatically as when we genetically manipulate cell size (Figure 1C). The inconsistency between our *ani-2* and embryogenesis experiments could be explained by a variety of factors. O-Mad2 may eventually become limiting in cells of the AB lineage with successive divisions after the two-cell stage, resulting in a greater reliance on PCH-2 function. Moreover, it may also suggest that relative levels of O-Mad2 and C-Mad2 are more stringently regulated as embryonic development progresses and the multicellular embryo becomes more complex. This possibility is supported by our finding that PCH-2 regulates normal cell cycle timing in $P_1$ cells, but not AB cells (Figure 5C), which implies that variations in O-Mad2/C-Mad2 ratios influence normal mitotic timing in cells with specific developmental fates. In addition, unlike the nuclei of two-cell embryos treated with *ani-2*$^{RNAi}$ (Supplemental Figure S3), nuclear volume scales with cell volume during embryogenesis (Gerhold *et al.*, 2018). Therefore, the concentration of Mad2 may not necessarily increase as cell size decreases in cells of the developing embryo, making direct comparisons between small cells obtained by *ani-2*$^{RNAi}$ treatment and small cells resulting from normal embryogenesis challenging. Finally, recent reports have indicated that, during embryogenesis in other systems, cell volume may not be a major contributor to spindle checkpoint strength (Chenevert *et al.*, 2019; Vazquez-Diez *et al.*, 2019). Indeed, in *C. elegans*, when only AB cells are monitored during very early embryogenesis (the two- to eight-cell stage), they exhibit very minor increases, if any, in checkpoint strength (Galli and Morgan, 2016; Gerhold *et al.*, 2018; Figure 4). This may suggest that cell fate is generally a more important determinant of spindle checkpoint strength during normal embryogenesis, potentially reconciling reports from a wide array of systems.

Our experiments identify CMT-1, the *C. elegans* ortholog of mammalian p31$^{comet}$, as an important regulator of PCH-2 function and, as a result, checkpoint strength. In addition to its requirement in facilitating PCH-2's ability to interact with its substrate, Mad2 (Miniowitz-Shemtov *et al.*, 2015; Ye *et al.*, 2015; Brulotte *et al.*, 2017; Alfieri *et al.*, 2018), CMT-1 localizes PCH-2 to unattached kinetochores (Nelson *et al.*, 2015) and promotes PCH-2's enrichment in $P_1$ cells (Figure 7D). We propose that both of these roles contribute to checkpoint strength. In large AB cells, CMT-1 ensures PCH-2's presence at unattached kinetochores, increasing the local concentration of O-Mad2, driving the production of soluble C-Mad2 and MCC and enforcing a robust checkpoint (Figure 8A). In $P_1$ cells, the combination of PCH-2's localization at kinetochores and its enrichment around chromosomes and near unattached kinetochores produces a checkpoint stronger than in somatic cells (Figure 8C). It is striking that, when CMT-1 is absent, AB cells, in which there is more PCH-2 (Figure 7D), and $P_1$ cells, which are slightly smaller than AB cells, exhibit similar checkpoint strength (Figure 7B). This indicates that even these cells depend on PCH-2 to be present at unattached kinetochores to increase the local concentration of O-Mad2 and promote checkpoint strength.

$P_1$ cells in both *pch-2;ani-2*$^{RNAi}$*;zyg-1*$^{RNAi}$ and *cmt-1;ani-2*$^{RNAi}$*;zyg-1*$^{RNAi}$ mutants show faster cell cycle timing than similarly sized AB cells of the same genotype (Figures 5B and 7A). However, only *pch-2* mutants significantly affect cell cycle timing in unperturbed $P_1$ cells (Figure 5C); $P_1$ cells in *cmt-1* and *mad-1* mutants show accelerated cell cycle timing but this is not significantly faster than control (Figures 5C and 7B). Further, we do not detect significant acceleration of the cell cycle in $P_1$ cells of *pch-2;zyg-1*$^{RNAi}$ or *mad-1;zyg-1*$^{RNAi}$ mutant embryos (Supplemental Figure S4 and Figure 7B). Given the rapidity of cell cycles in these early embryos, it is possible that *ani-2*$^{RNAi}$*;zyg-1*$^{RNAi}$ experiments provide greater sensitivity to observe subtle accelerations in cell cycle timing and that some subset of spindle checkpoint components, including PCH-2, CMT-1, MAD-1, and MAD-2 regulate normal cell cycle timing in germline precursor cells, similarly to the role of MAD-1 and MAD-2 in germline mitotic nuclei (Gerhold *et al.*, 2015). Unfortunately, we cannot test this with MAD-1 or MAD-2, since *mad-1* and *mad-2* mutants abolish the spindle checkpoint response in *ani-2*$^{RNAi}$*;zyg-1*$^{RNAi}$ embryos (Gerhold *et al.*, 2015 and Figure 1C). An alternative hypothesis that we do not favor is that only PCH-2 regulates cell cycle timing in $P_1$ cells, in a mechanism independent of other spindle checkpoint proteins.

Evolutionary analysis across phyla has revealed a close coevolutionary relationship between PCH-2 and its orthologs and HORMA domain–containing proteins, including CMT-1 and Mad2 (Vleugel *et al.*, 2012; van Hooff *et al.*, 2017). However, some organisms that rely on the templated conversion of O-Mad2 to C-Mad2 to assemble the MCC, such as budding and fission yeasts (Nezi *et al.*, 2006; Chao *et al.*, 2012), either do not express their PCH-2 ortholog during mitosis (budding yeast; San-Segundo and Roeder, 1999) or do not have a PCH-2 ortholog in their genome (fission yeast; Wu and Burgess, 2006). This is potentially explained by cell volume: both budding and fission yeasts are two orders of magnitude smaller than mammalian cells and *C. elegans* embryos. They also undergo closed mitosis, in which the nuclear envelope does not break down, providing an additional opportunity to concentrate factors required for mitosis. We propose that recruiting O-Mad2 to unattached kinetochores may not present as great a challenge in these significantly smaller cells, making a factor required to increase the local concentration of O-Mad2 at unattached kinetochores unnecessary.

An obvious question our experiments raise is how PCH-2 is enriched in $P_1$ cells. Germline precursor cells are transcriptionally silent until gastrulation (Seydoux *et al.*, 1996) and sequencing of mRNA in early embryos shows that neither CMT-1 nor PCH-2 mRNA is enriched in germline precursor cells (Tintori *et al.*, 2016), indicating that enrichment of PCH-2 is likely to occur at the level of protein regulation. Understanding this regulation, its control by developmental events and its effect on the relative levels of O-Mad2 and C-Mad2 in different cell types promise to be an exciting area of investigation.

## MATERIALS AND METHODS

### Worm strains

The *C. elegans* Bristol N2 (Brenner, 1974) was used as the wild-type strain. Most strains were maintained at 20°C, except for *zyg-1(or297)* strains, which were maintained at 15°C. See Supplemental Table S1 for the list of all the strains used in this study.

### Immunostaining

Immunostaining was performed on adult worms 48 h after L4, as described in Bhalla and Dernburg (2005). The antibodies used were rabbit anti-MAD-2 (1/500; Essex *et al.*, 2009) and mouse anti-MAb414 (1/400; Davis and Blobel, 1986). Secondary antibodies were Alexa Fluor 488 anti-rabbit (Invitrogen) and Cy3 anti-mouse (Jackson ImmunoResearch Laboratories) diluted at 1:500. Antibody against MAD-2 was a gift from A. Desai (Ludwig Institute/University of California, San Diego, La Jolla, CA).

Images were acquired on a DeltaVision Personal DV microscope (GE Healthcare) equipped with a 100 × NA 1.40 oil-immersion objective (Olympus) and a short ARC xenon lamp (GE Healthcare) and using a CoolSNAP charge-coupled camera (Roper Scientific). Z-stacks were collected at Z-spacing 0.2 µm and processed by constrained, iterative deconvolution. Imaging, image scaling, and analysis were performed using functions in the softWoRx software package (GE Healthcare). Projections were calculated by a maximum intensity algorithm. Composite images were assembled and some false coloring was performed with Fiji.

### Live imaging of two-cell embryos

For live imaging of two-cell embryos, worms were dissected on glass coverslips in egg buffer and then mounted on 2% agar pads. Images were acquired every 1 min or 20 s on a DeltaVision Personal DV microscope as described in the previous section; except that the distance between two planes was 2 µm. Mitotic timing was measured from NEBD to OCC as described in Nelson *et al.* (2015). Cell volumes were measured as described in Galli and Morgan (2016). To measure the nuclear area, a sum projection of the embryo was generated 1 min before chromosomes began to condense and the area was measured with Fiji (Supplemental Figure S3A).

### Live imaging of embryogenesis

After treatment with *perm-1*$^{RNAi}$ (see below), worms were dissected onto a coverslip with egg salt buffer (118 mM NaCl, 48 mM KCl) supplemented with 10 mM PIPES pH 7.3, 1 mM ATP, and 10 mM sucrose. Embryos and adult carcasses were transferred into a well of an eight-well plate (ibidi 1 µ-Slide 8 Well Glass bottom) that had been freshly coated with 0.1% poly-L-lysine solution (Sigma P8920) and washed extensively. Time-lapse videos were acquired with a Solamere spinning disk confocal system piloted by µManager software (Edelstein *et al.*, 2014) and equipped with a Yokogawa CSUX-1 scan head, a Nikon (Garden City, NY) TE2000-E inverted stand, a Hamamatsu ImageEM × 2 camera, LX/MAS 489 nm and LS/MAS 561 nm lasers, and a Plan Apo × 60/1.4 numerical aperture oil objective. Acquisition times per frame were 50 ms using 5% of the lasers' power for both channels, and images were obtained as stacks of planes at 2-µm intervals taken every 1 min. Nocodazole was added from a 5X stock to a final concentration of 50 µM after the first time point. Mitotic timing was measured from NEBD to DECON as described in Essex *et al.* (2009).

To image embryogenesis in *zyg-1(or297)* mutants, images were generated under the same conditions as described previously for the live imaging of two-cell embryos with a few modifications: images were acquired every 20 s on a DeltaVision Personal DV microscope in a room heated to 26°C. Mitotic timing was measured from NEBD to DECON as described in Essex *et al.* (2009).

### Quantification of fluorescence intensity

To quantify GFP::MAD-2 and PCH-2::GFP levels, images were generated under the same conditions as described previously for the live imaging of two-cell embryos with a few modifications: only the area defined by the GFP cloud and mitotic chromosomes was imaged, the interval between the four planes was 1 µm, and images were collected every 20 s. Quantification of fluorescence at kinetochores was performed in Fiji as described in Moyle *et al.* (2014) and Nelson *et al.* (2015). Briefly, maximum-intensity projections of both mCh::H2B and GFP fusion proteins were made after the pseudo-metaphase plate was generated. The image was rotated so that the metaphase plate was vertical, channels were split, and the maximum GFP pixel was identified using the process function within a box on the unattached side of the metaphase plate. In the same *x*-plane, the maximum mCh::H2B pixel was found. The width was changed to 12 pixels and the maximum GFP signal intensity was recorded in this 12-pixel window centered at the mCherry maxima. The background GFP signal was calculated by taking the average GFP intensity of a four-pixel box in the same *x*-plane, eight pixels away from the maximum mCherry on the opposite side of the pseudo-metaphase plate to the maximum GFP (i.e., the attached side). This background GFP was then subtracted from the maximum to measure the kinetochore bound GFP fusion intensity. Fluorescence around mitotic chromosomes was quantified as described in Galli and Morgan (2016). Sum intensity projections were generated and fluorescence in the area around mitotic chromosomes was measured in Fiji. Background fluorescence was measured in a 30-pixel band around this "cloud" and subtracted from the initial fluorescence intensity to determine the final fluorescence value. In some of our movies, identifying a clear metaphase plate was more difficult in AB than in $P_1$ cells. Therefore, to ensure that we were quantifying PCH-2::GFP fluorescence around mitotic chromosomes at the same stage in mitosis in these two cell types, PCH-2::GFP was quantified in frames that were normalized relative to NEBD and mitotic exit. To measure the cell volume, one Z-stack of the entire cell was taken at NEBD at Z-spacing 2 µm.

### Feeding RNA interference (RNAi)

*C. elegans* strains were fed HT115 bacteria expressing the desired dsRNA after IPTG induction. Bacterial strains containing RNAi vectors were cultured overnight at 37°C and centrifuged, and the pellet was resuspended in 1/50 of the original volume. Concentrated culture (100 µl) was spotted onto a nematode growth medium plate containing 1 mM IPTG and 50 µg/µl of kanamycin or carbenicillin and the plate was incubated overnight at 37°C.

For *ani-2* RNAi, gravid adults were bleached onto the RNAi plate and their progeny were allowed to develop at 20°C for 2.5 d. Then L4s were transferred to a fresh plate containing OP50 or *zyg-1* RNAi bacteria.

For *zyg-1* RNAi, L4s were transferred from an OP50 or *ani-2* RNAi plate onto a *zyg-1* RNAi plate and cultured at 20°C for 1.5 d.

For *perm-1* RNAi, young adults (8 h post-L4) were incubated on *perm-1* RNAi plates at 15°C for 16–20 h.

For *par-1*, *par-6*, and *gpr-1/2* RNAi, gravid adults were bleached onto control RNAi (L4440) plates and their progeny were allowed to develop at 15°C for 3 d. L4s were then transferred onto *par-1*, *par-6*, or *gpr-1/2* RNAi or control RNAi plates and incubated at 15°C for 3 d. For *gpr-1/2* RNAi, "small" AB cells were identified by whether their area was at least one SD lower than the average of control AB cells and "large" $P_1$ cells were identified by whether their area was at least one SD higher than the average of control $P_1$ cells.

### Statistical Analysis

All statistical analysis was performed using GraphPad Prism version 6 for Macintosh, including linear regression analysis and assessing the significance of these data (Figures 1C, 2B, 3C, 5A, B, and 7A and Supplemental Figure S1, C and D). In comparing two means, significance was assessed by performing two-tailed *t* tests (Figure 6C and Supplemental Figures S5, B and D, S6, B–D, and S7A). In graphs in which multiple means were tested, we performed ANOVA analysis with the Sidak post hoc test (Figures 1D, 5C, 6, A and E, and 7, B and D, and Supplemental Figures S4A and S8, A, B, and D). In all graphs, a * indicates $p < 0.05$, ** indicates $p < 0.01$, and *** $p < 0.0001$.

## ACKNOWLEDGMENTS

We would like to thank Arshad Desai, Karen Oegema, Susan Strome, and David Morgan for valuable strains and reagents. This work was supported by the NIH (Grants T32GM008646 [C.R.N. and A.R.] and R01GM097144 [N.B.]). Some strains were provided by the CGC, which is funded by NIH Office of Research Infrastructure Programs (P40 OD010440).

## REFERENCES

Alfieri C, Chang L, Barford D (2018). Mechanism for remodeling of the cell cycle checkpoint protein MAD2 by the ATPase TRIP13. Nature 559, 274–278.

Aravind L, Koonin EV (1998). The HORMA domain: a common structural denominator in mitotic checkpoints, chromosome synapsis and DNA repair. Trends Biochem Sci 23, 284–286.

Bhalla N, Dernburg AF (2005). A conserved checkpoint monitors meiotic chromosome synapsis in Caenorhabditis elegans. Science 310, 1683–1686.

Bohr T, Nelson CR, Klee E, Bhalla N (2015). Spindle assembly checkpoint proteins regulate and monitor meiotic synapsis in C. elegans. J Cell Biol 211, 233–242.

Brenner S (1974). The genetics of *Caenorhabditis elegans*. Genetics 77, 71–94.

Brulotte ML, Jeong BC, Li F, Li B, Yu EB, Wu Q, Brautigam CA, Yu H, Luo X (2017). Mechanistic insight into TRIP13-catalyzed Mad2 structural transition and spindle checkpoint silencing. Nat Commun 8, 1956.

Carvalho A, Olson SK, Gutierrez E, Zhang K, Noble LB, Zanin E, Desai A, Groisman A, Oegema K (2011). Acute drug treatment in the early *C. elegans* embryo. PLoS One 6, e24656.

Chao WC, Kulkarni K, Zhang Z, Kong EH, Barford D (2012). Structure of the mitotic checkpoint complex. Nature 484, 208–213.

Chen RH, Shevchenko A, Mann M, Murray AW (1998). Spindle checkpoint protein Xmad1 recruits Xmad2 to unattached kinetochores. J Cell Biol 143, 283–295.

Chen RH, Waters JC, Salmon ED, Murray AW (1996). Association of spindle assembly checkpoint component XMAD2 with unattached kinetochores. Science 274, 242–246.

Chenevert J, Roca M, Besnardeau L, Ruggiero A, Nabi D, McDougall A, Copley RR, Christians E, Castagnetti S (2019). The spindle assembly checkpoint functions during early development in non-chordate embryos. bioRxiv.

Collin P, Nashchekina O, Walker R, Pines J (2013). The spindle assembly checkpoint works like a rheostat rather than a toggle switch. Nat Cell Biol 15, 1378–1385.

Colombo K, Grill SW, Kimple RJ, Willard FS, Siderovski DP, Gonczy P (2003). Translation of polarity cues into asymmetric spindle positioning in *Caenorhabditis elegans* embryos. Science 300, 1957–1961.

Date DA, Burrows AC, Summers MK (2014). Phosphorylation regulates the p31Comet-mitotic arrest-deficient 2 (Mad2) interaction to promote spindle assembly checkpoint (SAC) activity. J Biol Chem 289, 11367–11373.

Davis LI, Blobel G (1986). Identification and characterization of a nuclear pore complex protein. Cell 45, 699–709.

De Antoni A, Pearson CG, Cimini D, Canman JC, Sala V, Nezi L, Mapelli M, Sironi L, Faretta M, Salmon ED, Musacchio A (2005). The Mad1/Mad2 complex as a template for Mad2 activation in the spindle assembly checkpoint. Curr Biol 15, 214–225.

Dick AE, Gerlich DW (2013). Kinetic framework of spindle assembly checkpoint signalling. Nat Cell Biol 15, 1370–1377.

Edelstein AD, Tsuchida MA, Amodaj N, Pinkard H, Vale RD, Stuurman N (2014). Advanced methods of microscope control using muManager software. J Biol Methods 1.

Essex A, Dammermann A, Lewellyn L, Oegema K, Desai A (2009). Systematic analysis in *Caenorhabditis elegans* reveals that the spindle checkpoint is composed of two largely independent branches. Mol Biol Cell 20, 1252–1267.

Eytan E, Wang K, Miniowitz-Shemtov S, Sitry-Shevah D, Kaisari S, Yen TJ, Liu ST, Hershko A (2014). Disassembly of mitotic checkpoint complexes by the joint action of the AAA-ATPase TRIP13 and p31(comet). Proc Natl Acad Sci USA 111, 12019–12024.

Fava LL, Kaulich M, Nigg EA, Santamaria A (2011). Probing the in vivo function of Mad1:C-Mad2 in the spindle assembly checkpoint. EMBO J 30, 3322–3336.

Galli M, Morgan DO (2016). Cell size determines the strength of the spindle assembly checkpoint during embryonic development. Dev Cell 36, 344–352.

Gerhold AR, Poupart V, Labbe JC, Maddox PS (2018). Spindle assembly checkpoint strength is linked to cell fate in the *Caenorhabditis elegans* embryo. Mol Biol Cell 29, 1435–1448.

Gerhold AR, Ryan J, Vallee-Trudeau JN, Dorn JF, Labbe JC, Maddox PS (2015). Investigating the regulation of stem and progenitor cell mitotic progression by in situ imaging. Curr Biol 25, 1123–1134.

Goldstein B, Macara IG (2007). The PAR proteins: fundamental players in animal cell polarization. Dev Cell 13, 609–622.

Gotta M, Dong Y, Peterson YK, Lanier SM, Ahringer J (2003). Asymmetrically distributed *C. elegans* homologs of AGS3/PINS control spindle position in the early embryo. Curr Biol 13, 1029–1037.

Guo S, Kemphues KJ (1995). par-1, a gene required for establishing polarity in *C. elegans* embryos, encodes a putative Ser/Thr kinase that is asymmetrically distributed. Cell 81, 611–620.

Habu T, Kim SH, Weinstein J, Matsumoto T (2002). Identification of a MAD2-binding protein, CMT2, and its role in mitosis. EMBO J 21, 6419–6428.

Hung TJ, Kemphues KJ (1999). PAR-6 is a conserved PDZ domain-containing protein that colocalizes with PAR-3 in *Caenorhabditis elegans* embryos. Development 126, 127–135.

Kim DH, Han JS, Ly P, Ye Q, McMahon MA, Myung K, Corbett KD, Cleveland DW (2018). TRIP13 and APC15 drive mitotic exit by turnover of interphase- and unattached kinetochore-produced MCC. Nat Commun 9, 4354.

Kitagawa R, Rose AM (1999). Components of the spindle-assembly checkpoint are essential in *Caenorhabditis elegans*. Nat Cell Biol 1, 514–521.

Kyogoku H, Kitajima TS (2017). Large Cytoplasm Is Linked to the Error-Prone Nature of Oocytes. Dev Cell 41, 287–298.e284.

Lara-Gonzalez P, Moyle MW, Budrewicz J, Mendoza-Lopez J, Oegema K, Desai A (2019). The G2-to-M transition is ensured by a dual mechanism that protects Cyclin B from degradation by Cdc20-activated APC/C. Dev Cell 51, 313–325.e310.

Lawrence KS, Chau T, Engebrecht J (2015). DNA damage response and spindle assembly checkpoint function throughout the cell cycle to ensure genomic integrity. PLoS Genet 11, e1005150.

Li Y, Benezra R (1996). Identification of a human mitotic checkpoint gene: hsMAD2. Science 274, 246–248.

Luo X, Tang Z, Rizo J, Yu H (2002). The Mad2 spindle checkpoint protein undergoes similar major conformational changes upon binding to either Mad1 or Cdc20. Mol Cell 9, 59–71.

Luo X, Tang Z, Xia G, Wassmann K, Matsumoto T, Rizo J, Yu H (2004). The Mad2 spindle checkpoint protein has two distinct natively folded states. Nat Struct Mol Biol 11, 338–345.

Ma HT, Poon RY (2016). TRIP13 regulates both the activation and inactivation of the spindle-assembly checkpoint. Cell Rep 14, 1086–1099.

Ma HT, Poon RYC (2018). TRIP13 Functions in the establishment of the spindle assembly checkpoint by replenishing O-MAD2. Cell Rep 22, 1439–1450.

Maddox AS, Habermann B, Desai A, Oegema K (2005). Distinct roles for two C. *elegans* anillins in the gonad and early embryo. Development 132, 2837–2848.

Mariani L, Chiroli E, Nezi L, Muller H, Piatti S, Musacchio A, Ciliberto A (2012). Role of the Mad2 dimerization interface in the spindle assembly checkpoint independent of kinetochores. Curr Biol 22, 1900–1908.

Marks DH, Thomas R, Chin Y, Shah R, Khoo C, Benezra R (2017). Mad2 overexpression uncovers a critical role for TRIP13 in mitotic exit. Cell Rep 19, 1832–1845.

Meraldi P, Draviam VM, Sorger PK (2004). Timing and checkpoints in the regulation of mitotic progression. Dev Cell 7, 45–60.

Miniowitz-Shemtov S, Eytan E, Kaisari S, Sitry-Shevah D, Hershko A (2015). Mode of interaction of TRIP13 AAA-ATPase with the Mad2-binding protein p31comet and with mitotic checkpoint complexes. Proc Natl Acad Sci USA 112, 11536–11540.

Moyle MW, Kim T, Hattersley N, Espeut J, Cheerambathur DK, Oegema K, Desai A (2014). A Bub1-Mad1 interaction targets the Mad1–Mad2 complex to unattached kinetochores to initiate the spindle checkpoint. J Cell Biol 204, 647–657.

Nelson CR, Hwang T, Chen PH, Bhalla N (2015). TRIP13PCH-2 promotes Mad2 localization to unattached kinetochores in the spindle checkpoint response. J Cell Biol 211, 503–516.

Nezi L, Rancati G, De Antoni A, Pasqualato S, Piatti S, Musacchio A (2006). Accumulation of Mad2-Cdc20 complex during spindle checkpoint

activation requires binding of open and closed conformers of Mad2 in *Saccharomyces cerevisiae*. J Cell Biol 174, 39–51.
Nystul TG, Goldmark JP, Padilla PA, Roth MB (2003). Suspended animation in *C. elegans* requires the spindle checkpoint. Science 302, 1038–1041.
O'Connell KF, Caron C, Kopish KR, Hurd DD, Kemphues KJ, Li Y, White JG (2001). The *C. elegans* zyg-1 gene encodes a regulator of centrosome duplication with distinct maternal and paternal roles in the embryo. Cell 105, 547–558.
O'Rourke SM, Carter C, Carter L, Christensen SN, Jones MP, Nash B, Price MH, Turnbull DW, Garner AR, Hamill DR, *et al*. (2011). A survey of new temperature-sensitive, embryonic-lethal mutations in *C. elegans*: 24 alleles of thirteen genes. PLoS One 6, e16644.
Rodriguez-Bravo V, Maciejowski J, Corona J, Buch HK, Collin P, Kanemaki MT, Shah JV, Jallepalli PV (2014). Nuclear pores protect genome integrity by assembling a premitotic and Mad1-dependent anaphase inhibitor. Cell 156, 1017–1031.
Rose L, Gonczy P (2014). Polarity establishment, asymmetric division and segregation of fate determinants in early *C. elegans* embryos. WormBook, 1–43.
Rosenberg SC, Corbett KD (2015). The multifaceted roles of the HORMA domain in cellular signaling. J Cell Biol 211, 745–755.
San-Segundo PA, Roeder GS (1999). Pch2 links chromatin silencing to meiotic checkpoint control. Cell 97, 313–324.
Seydoux G, Mello CC, Pettitt J, Wood WB, Priess JR, Fire A (1996). Repression of gene expression in the embryonic germ lineage of *C. elegans*. Nature 382, 713–716.
Simonetta M, Manzoni R, Mosca R, Mapelli M, Massimiliano L, Vink M, Novak B, Musacchio A, Ciliberto A (2009). The influence of catalysis on mad2 activation dynamics. PLoS Biol 7, e10.
Sironi L, Mapelli M, Knapp S, De Antoni A, Jeang KT, Musacchio A (2002). Crystal structure of the tetrameric Mad1–Mad2 core complex: implications of a "safety belt" binding mechanism for the spindle checkpoint. EMBO J 21, 2496–2506.
Sironi L, Melixetian M, Faretta M, Prosperini E, Helin K, Musacchio A (2001). Mad2 binding to Mad1 and Cdc20, rather than oligomerization, is required for the spindle checkpoint. EMBO J 20, 6371–6382.
Srinivasan DG, Fisk RM, Xu H, van den Heuvel S (2003). A complex of LIN-5 and GPR proteins regulates G protein signaling and spindle function in *C. elegans*. Genes Dev 17, 1225–1239.
Stein KK, Davis ES, Hays T, Golden A (2007). Components of the spindle assembly checkpoint regulate the anaphase-promoting complex during meiosis in *Caenorhabditis elegans*. Genetics 175, 107–123.
Sudakin V, Chan GK, Yen TJ (2001). Checkpoint inhibition of the APC/C in HeLa cells is mediated by a complex of BUBR1, BUB3, CDC20, and MAD2. J Cell Biol 154, 925–936.
Teichner A, Eytan E, Sitry-Shevah D, Miniowitz-Shemtov S, Dumin E, Gromis J, Hershko A (2011). p31comet promotes disassembly of the mitotic checkpoint complex in an ATP-dependent process. Proc Natl Acad Sci USA 108, 3187–3192.
Tintori SC, Osborne Nishimura E, Golden P, Lieb JD, Goldstein B (2016). A transcriptional lineage of the early *C. elegans* embryo. Dev Cell 38, 430–444.
Tipton AR, Wang K, Oladimeji P, Sufi S, Gu Z, Liu ST (2012). Identification of novel mitosis regulators through data mining with human centromere/kinetochore proteins as group queries. BMC Cell Biol 13, 15.
Vader G (2015). Pch2(TRIP13): controlling cell division through regulation of HORMA domains. Chromosoma 124, 333–339.
van Hooff JJ, Tromer E, van Wijk LM, Snel B, Kops GJ (2017). Evolutionary dynamics of the kinetochore network in eukaryotes as revealed by comparative genomics. EMBO Rep.
Vazquez-Diez C, Paim LMG, FitzHarris G (2019). Cell-size-independent spindle checkpoint failure underlies chromosome segregation error in mouse embryos. Curr Biol 29, 865–873.e863.
Vleugel M, Hoogendoorn E, Snel B, Kops GJ (2012). Evolution and function of the mitotic checkpoint. Dev Cell 23, 239–250.
Wang K, Sturt-Gillespie B, Hittle JC, Macdonald D, Chan GK, Yen TJ, Liu ST (2014). Thyroid hormone receptor interacting protein 13 (TRIP13) AAA-ATPase is a novel mitotic checkpoint-silencing protein. J Biol Chem 289, 23928–23937.
Westhorpe FG, Tighe A, Lara-Gonzalez P, Taylor SS (2011). p31comet-mediated extraction of Mad2 from the MCC promotes efficient mitotic exit. J Cell Sci 124, 3905–3916.
Wu HY, Burgess SM (2006). Two distinct surveillance mechanisms monitor meiotic chromosome metabolism in budding yeast. Curr Biol 16, 2473–2479.
Xia G, Luo X, Habu T, Rizo J, Matsumoto T, Yu H (2004). Conformation-specific binding of p31(comet) antagonizes the function of Mad2 in the spindle checkpoint. EMBO J 23, 3133–3143.
Ye Q, Rosenberg SC, Moeller A, Speir JA, Su TY, Corbett KD (2015). TRIP13 is a protein-remodeling AAA+ ATPase that catalyzes MAD2 conformation switching. eLife 4.
Yost S, de Wolf B, Hanks S, Zachariou A, Marcozzi C, Clarke M, de Voer RM, Etemad B, Uijttewaal E, Ramsay E, *et al*. (2017). Biallelic TRIP13 mutations predispose to Wilms tumor and chromosome missegregation. Nat Genet.